POLYTECHNIC OF TURIN

Master's Degree in Aerospace Engineering

Politecnico di Torino

大阪大学
THE UNIVERSITY OF OSAKA

Master's Degree Thesis

Large-eddy Simulation on the Cavitating Turbulent Flow around a Hydrofoil Considering the Cavity Generation from SGS Vortices

Supervisors

Prof. Domenic D'AMBROSIO

Prof. Kie OKABAYASHI

Prof. Shintaro TAKEUCHI

Candidate

Valentina COLLESEI

31 March 2026

Abstract

The subject of this project is the analysis of Large Eddy Simulation (LES) results using a new cavitation model that accounts for the influence of cavities generated by turbulent vortices in the sub-grid scale, which are often approximated using eddy viscosity in LES models. This is achieved by implementing a probabilistic approach (PDF model) that bridges the gap between the filtered pressure field and the local microscopic pressure drops.

The research is divided into two main computational setups. In the first case, characterized by a moderate angle of attack, the study demonstrates how the inclusion of SGS pressure fluctuations significantly improves the prediction of the sheet-to-cloud cavitation transition, which is often underestimated by conventional models. The second case explores a flow regime with a higher angle of attack, where the interaction between turbulent detachment and cavitation becomes dominant. The results are compared against experimental data and standard No PDF simulations to assess the sensitivity of the model and the calibration of the model constant. The findings highlight that accounting for SGS turbulence is essential for a more physically consistent representation of the cavitation inception and shedding frequency, however the model is unable to improve significantly the results for the second case analyzed, highlighting the complexity of the phenomenon under study.

Table of Contents

List of Tables IV

List of Figures V

1 Introduction 1
- 1.1 Numerical approaches and challenges . . . 1
- 1.2 Types of cavitation . . . 2
- 1.3 Classification and review of cavitation models . . . 3
- 1.4 Turbulence modeling for cavitation . . . 4
- 1.5 Goal and structure of the thesis . . . 5

2 Overview of Computation 7
- 2.1 Governing equations . . . 7
  - 2.1.1 Mass Conservation . . . 8
  - 2.1.2 Momentum Conservation . . . 8
- 2.2 SGS model . . . 9
- 2.3 Baseline cavitation model . . . 10
- 2.4 PDF-based model . . . 11
- 2.5 Numerical scheme . . . 15
- 2.6 Computational setup and target of analysis . . . 17
- 2.7 Domain decomposition for post-processing . . . 20

3 Results and discussion for Case 1 22
- 3.1 Cell Volume . . . 22
- 3.2 Pressure Distribution . . . 26
- 3.3 Lift and Drag Distribution . . . 28
- 3.4 Turbulent Energy formation . . . 37
- 3.5 Sheet Cavity Length . . . 40
- 3.6 Cell Volume at the Leading Edge . . . 43

4 Results and discussion for Case 2 45
4.1 Cell Volume 45
4.2 Lift and Drag distribution 49
4.3 Cell Volume at the trailing edge 56

5 Conclusions 58
5.1 Effectiveness of the PDF model 58
5.2 Limitations 59
5.3 Considerations regarding C 59
5.4 Possible future developments 60
5.5 Final remarks 60

Bibliography 62

List of Tables

2.1 Flow parameters for the two profiles. 20

3.1 Mean values of C_L and C_D for the three models 30
3.2 Parameters of the FFT analysis 32
3.3 Relationship $L_{\max}/c$ for different PDF cases 41
3.4 Behaviours of cavitation at various cavitation numbers for $\alpha = 8°$. 42

4.1 Parameters of the FFT analysis 55

List of Figures

1.1 Different cavitating phenomena 2
1.2 Vortex cavitation in the strong shear layer $\alpha = 19°$ and $\sigma = 1.67$ [10] 3

2.1 Various forms of PDF 11
2.2 Basic concept of Gaussian pressure distribution 12
2.3 Gaussian distribution 14
2.4 Behaviour of cavitation 17
2.5 Boundary conditions [1] 18
2.6 Mesh 19
2.7 Mesh around the profile 19
2.8 Domain division 20

3.1 Cavity generation for $C = 5$. 23
3.2 Cavity generation for $C = 10$. 24
3.3 Cavity generation at a given time step for $C = 5$. 24
3.4 Cavity generation at a given time step for $C = 10$. 25
3.5 Comparison between experimental and CFD pressure distributions, adapted from [1]. 26
3.6 Pressure coefficient distribution for the different models. 27
3.7 Zoomed view near the leading edge. 27
3.8 Lift and drag coefficients for the case without the PDF model. . . . 28
3.9 Lift and drag coefficients for the PDF model with $C = 5$. 29
3.10 Lift and drag coefficients for the PDF model with $C = 10$. 29
3.11 FFT spectrum for the No-PDF model. 31
3.12 FFT spectrum for the PDF model with $C = 5$. 31
3.13 FFT spectrum for the PDF model with $C = 10$. 32
3.14 Cavity cycle for No-PDF case 34
3.15 Cavitation cycle and C_L value for C=5 case 35
3.16 Cavitation cycle and C_L value for C=10 case 36
3.17 Cavity and SGS turbulent kinetic energy for C=5 case and $(z/C = 0.2)$ 38

3.18 Cavity and SGS turbulent kinetic energy for C=10 case and ($z/C = 0.2$) . . . 39
3.19 Maximum sheet cavity length for found with various models 40
3.20 No PDF case . . . 40
3.21 PDF C= 5 case . . . 41
3.22 PDF C=10 case . . . 41
3.23 Cell Volume and K_{SGS} at the Leading Edge for the C=5 case . . . 43
3.24 Cell Volume and K_{SGS} at the Leading Edge for the C=10 case . . . 44

4.1 Cavity generation for $C = 5$ . . . 46
4.2 Cavity generation for $C = 10$ . . . 47
4.3 Cavity generation for $C = 10$ and $\Delta t = 2.5 \times 10^{-6} s$ . . . 48
4.4 Cavity pattern of the experimental data during a few cycles of cavity oscillation $\alpha = 20°$, $\sigma = 2.7$ [49] . . . 49
4.5 Cavitation cycle for the No PDF $\Delta t = 2.5 \times 10^{-6}$ case . . . 50
4.6 C_L and C_D values for the No PDF and $\Delta t = 2.5 \times 10^{-6}$ case . . . 50
4.7 Cavitation cycle for C=5 case . . . 51
4.8 C_L and C_D values for C=5 . . . 51
4.9 C_L and C_D values for the C=10 $\Delta t = 5 \times 10^{-6}$ . . . 52
4.10 C_L and C_D values for the C=10 $\Delta t = 2.5 \times 10^{-6}$ . . . 53
4.11 FFT No PDF $\Delta t = 2.5 \times 10^{-6}$ . . . 53
4.12 FFT C=5 . . . 54
4.13 FFT C=10 $\Delta t = 2.5 \times 10^{-6}$ . . . 54
4.14 Cavity volume generation and K_{SGS} at the trailing edge for $C = 5$ . . . 56
4.15 Cavity volume generation and K_{SGS} at the trailing edge for $C = 10$ $\Delta t = 2.5 \times 10^{-6}$ . . . 57

Acronyms

BC
Boundary Conditions.

CFD
Computational Fluid Dynamics.

DES
Detached Eddy Simulation.

DNS
Direct Numerical Simulation.

DSM
Dynamic Smagorinsky Model.

FFT
Fast Fourier Transform.

GS
Grid Scale.

LES
Large Eddy Simulation.

PDF
Probability Density Function.

PSD
Power Spectral Density.

RANS

Reynolds-Average Navier-Stokes.

SGS

Sub-Grid Scale.

Chapter 1

Introduction

Cavitation is a widespread phenomenon that occurs in various contexts, such as pumps, propellers, and hydrofoils [1]. It happens when the pressure in a specific region of liquid falls below the saturated vapor pressure causing the liquid to transition into vapor, which results in the formation of cavities within the liquid [2]. The adverse effects of cavitation include reductions in the performance of fluid machinery, erosion of solid surfaces due to the high pressures generated during bubble collapse, and production of vibrations and noise [3]. Cavitating flows are commonly encountered in engineering applications, and the difficulty in accurately predicting their behavior represents a significant challenge for modern engineering [4].

Over the years, research on cavitation has focused primarily on its suppression and control. Recently, however, a stronger interest towards the active utilization of the phenomenon is occurring. Cavitation can, indeed, be exploited for purposes such as cleaning, surface treatment, enhancement of chemical reactions [5], elimination of harmful microorganisms [6], and various medical applications[7], [8]. This is why contemporary studies on cavitation encompass a broad range of perspectives, from suppression and control to effective utilization of the phenomenon [4].

1.1 Numerical approaches and challenges

In general conducting experimental performance tests on fluid machinery is costly and the use of liquid fuels in such experiments can be hazardous and impractical [4]. Conversely, numerical simulations are more cost-effective and allow for performance evaluation under varying parameters and geometries easily. For this reason, numerical approaches are increasingly used for the development of equipment subject to cavitating flows.

Cavitation is a process in which small gas bubbles containing non-condensable

gases within a liquid rapidly grow, contract, and collapse due to pressure fluctuations in the flow field. The characteristic time scale of bubble dynamics is typically much shorter than that of the surrounding flow, and the spatial scales of the bubbles and the flow field also differ substantially. As a result, cavitating flows exhibit strong unsteady behavior across multiple temporal and spatial scales. The accurate estimation of small-scale cavities can be as important as that of large-scale structures [9]. Because of this complex behavior, cavitation flows are still an significant challenge in numerical simulation.

1.2 Types of cavitation

Cavitating flows are usually classified into five main categories: bubble, sheet, cloud, vortex, and super-cavitation. Bubble cavities occur when the cavitation consists of discrete bubbles that move downstream and collapse in regions of higher pressure. A sheet cavity, on the other hand, is attached to the surface of the hydrofoil and presents a clear interface between the liquid and vapor phases. A cloud cavity is formed by the coalescence of small bubbles, usually separating from an initial sheet cavity. Finally, a super-cavity consists of a large cavity that goes around the entire body, or at least most of it. Apart from these primary types of cavitating patterns, secondary effects such as re-entrant jets, turbulence, and interactions between bubbles and solid surfaces can further complicate the flow structures.[2] A schematic example of the main phenomena occurring around a hydrofoil subject to cavitation can be seen in Fig. 1.1.

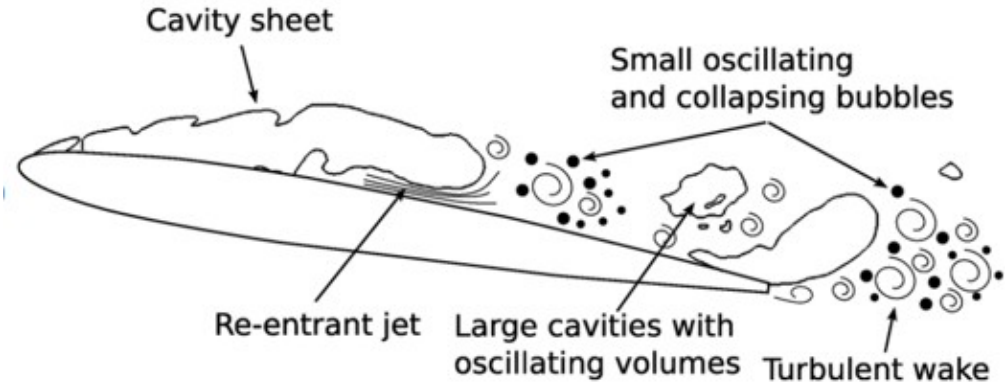

Figure 1.1: Different cavitating phenomena

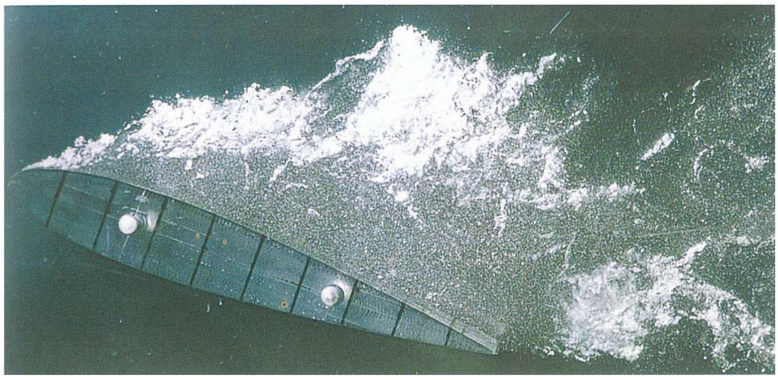

Figure 1.2: Vortex cavitation in the strong shear layer $\alpha = 19°$ and $\sigma = 1.67$ [10]

Fig.1.2, on the other hand, displays vortex cavitation occurring around a hydrofoil in the strong shear layer when $\alpha = 19°$ and $\sigma = 1.67$.

1.3 Classification and review of cavitation models

Since the 1980s, Navier–Stokes-based methods have been developed for analyzing cavitating flows. The cavitation models used in such analyses can generally be categorized into two main types: the single-fluid model, which treats the two-phase mixture as a homogeneous medium and neglects slip velocities between the phases, and the two-fluid model, which solves separate governing equations for the liquid and vapor phases [4]. Currently, however, a unique CFD method applicable to all types of cavitation has not been created. The most appropriate method is strongly dependent on the cavitation regime under study.

In homogeneous single-fluid models, the gas–liquid mixture is treated as a single fluid whose density depends on the vapor volumetric fraction and liquid volumetric fraction. Several formulations are based on this principle. For instance, equation of state models determine mixture density based solely on pressure [11], while transport-equation models introduce mass-transfer source terms for evaporation and condensation, as in the models of Merkle et al.[12], Kunz et al. [13], Singhal et al. [14], Schnerr–Sauer et al.[15], and Zwart et al.[16]. Other approaches rely on simplified bubble-dynamics equations, where the vapor volume fraction is obtained from Rayleigh–Plesset type expressions with a prescribed bubble number density [17]. These homogeneous fluid models are widely employed because of their simplicity and relatively low computational cost.

Two-fluid models, on the other hand, treat liquid and vapor as separate phases with distinct velocities. Eulerian formulations solve transport equations for both phases [18], whereas Lagrangian models track vapor bubbles individually. Although

these models can represent bubble-scale dynamics more accurately, they are computationally expensive and the conversion between structures at different length scales, including bubble coalescence and fragmentation, proved to be difficult [19].

Despite the wide variety of available models, none of them can accurately reproduce all cavitation regimes within a single unified framework. Even for standard hydrofoils, many models struggle to capture sheet cavity length, interface dynamics, and the unsteady behavior observed in experiments. This limitation is commonly attributed to the fact that different cavitation mechanisms dominate in different flow regions, making a single model formulation insufficient to represent the entire phenomenon [20]. Although the choice of a cavitation model determines how the phase change is represented, the overall predictive accuracy of a simulation also depends strongly on the turbulence modeling strategy. Turbulence influences cavity formation, growth, and shedding, and therefore an appropriate treatment of both resolved and sub-grid-scale (SGS) motions is essential for accurately capturing cavitating flows.

1.4 Turbulence modeling for cavitation

Different turbulence models have been employed to study cavitating flows so far, including Reynolds-Averaged Navier-Stokes (RANS) [21] and Large Eddy Simulation (LES)[22]. RANS approaches are unable to adequately capture the strong unsteadiness characteristic of cavitating turbulence. Moreover, RANS solutions tend to depend heavily on the specific turbulence model adopted. During international benchmark studies on cavitating hydrofoils, it has been shown that unsteady Reynolds-averaged numerical simulation (URANS) tends to excessively smooth turbulent fluctuations, leading to an underestimation of sheet cavity length and to an inaccurate prediction of lift breakdown [23]. Improvements such as modified vapor pressure [22], density-dependent eddy viscosity[24], or cavitation-induced source terms[25] have been proposed, but they often rely on empirical parameters.

Large-Eddy Simulation (LES), on the other hand, has progressively become a more suitable approach for dynamic cavitating flows, as it resolves the large-scale vortical structures responsible for cavity formation, shedding, and re-entrant jet dynamics. LES models, indeed, are based on the principle that large vortices with low wave numbers are dependent on the flow field, whereas small vortices with high wave numbers exhibit more universal behavior and are thus modeled using turbulence models. Several LES investigations have successfully reproduced key features of unsteady cavitation, including cloud shedding and spanwise interface instabilities. At present, most LES models are based on the Smagorinsky model and its dynamic variant, which were originally developed for single-phase flows [26].

For instance, Qin & Wosnik [27],[28] analyzed two-dimensional cavitating flow around a NACA0015 wing profile using a model that assumed a barotropic fluid, with the approximation of weak compressibility and the Smagorinsky model with the van Driest function [29] at the wall boundary. This research showed a strong correlation between cloud cavity shedding, trailing-edge vortex release and lift fluctuations and good agreement with the experimental results found through PIV measurements. Similarly, Wang & Ostoja-Starzewski [30], performed computations using a similar cavitation and turbulence model for a hydrofoil and successfully reproduced sheet cavitation and periodic cloud cavity shedding. Also Yamada et al. [31] conducted LES of flows around basic shapes using the model proposed by Okita and Kajima [32] and the Dynamic Smagorinsky model (DMS)[26]. They were able to obtain good lift to drag ratios but failed to reproduce unsteady phenomena like re-entrant jet and cloud cavity release and speculated that this was probably due to an underestimation of the eddy viscosity. Both Shams & Apte [33] and Liu & Katz [34] analyzed cavitation in the same open cavity with a cavitation model using a two-fluid model and a transport equation model combined with the DSM. Several other simulations of cavitating flows were carried out using the Smagorinsky model throughout the years [35],[36],[37]. In some of which, like Suzuki et al.[38] and Pendar & Roohi [39] LES models were utilized in commercial software.
Hybrid methods such as detached-eddy simulation (DES) have also been employed, although their accuracy strongly depends on near-wall resolution. DES combines RANS and LES for high Reynolds number flows: the boundary layer along the wall is handled with RANS, and the detached flow is treated with LES. An advantage of this method is that it requires less computational resources than LES but so far no modifications have been made to account for cavitation. For example, Ugajin [40] deployed the cavitation model developed by Okita &Kajijama [32] together with a basic DES model by Spalart [41] for turbulence modeling giving physically valid results but without obtaining clear improvements.

1.5 Goal and structure of the thesis

Despite extensive experimental evidence that cavitation is initiated in the cores of fine-scale turbulent vortices, most existing numerical simulations based on LES or DES resolve only large-scale motions and model small-scale vortices statistically. As a result, the strong, highly localized low-pressure events that occur in SGS vortices and act as the primary sources of cavitation cannot be represented explicitly. This limitation makes it difficult to reproduce the onset of vortex cavitation and its subsequent interaction with turbulence within conventional single-phase turbulence frameworks. Therefore, a modeling approach in which SGS vortices are allowed to directly generate cavitation, and in which the mutual interaction between cavitation

and SGS turbulence is consistently taken into account, is essential for the physically accurate simulation of unsteady cavitating turbulent flows.

The goal of this study is to evaluate the performance of a LES framework incorporating a probability density function (PDF)–based cavitation model designed to account for these unresolved pressure fluctuations. Since conventional LES filters out local pressure depressions induced by SGS vortices, an improved formulation capable of incorporating their statistical effect is required. A PDF-based approach allows the distribution of instantaneous pressure within each computational cell to be represented, enabling cavitation to occur even when the filtered pressure remains above the vapor pressure. The analysis focuses on the cavitating flow around a Clark-Y11.7% hydrofoil under two operating conditions, with the aim of determining whether the proposed model improves the prediction of sheet cavity length, pressure distribution, and unsteady dynamics compared to a standard LES formulation.

This thesis is organized as follows. Chapter 2 presents an overview of the computational model, including the governing equations, cavitation model, numerical scheme, and computational setup. Chapters 3 and 4 discuss the results for the two operating conditions. Finally, Chapter 5 presents the conclusions.

Chapter 2

Overview of Computation

2.1 Governing equations

Since the liquid phase is regarded as a weakly compressible fluid and the mean flow is characterized by a relatively low Mach number, an incompressible-type formulation based on the low Mach number approximation is employed. This approach allows for the treatment of slight compressibility effects without the computational cost associated with fully compressible solvers, while still accounting for pressure–density coupling that drives cavitation inception [4].

All variables appearing in the governing equations are non-dimensionalized using reference quantities: a characteristic length c, the freestream velocity u_∞, and the far-field liquid density $\rho_{L\infty}$. The kinematic viscosity of the liquid phase is assumed to be constant throughout the domain, which is a reasonable assumption considering the small temperature variations typically associated with hydrodynamic cavitation.

The cavitating flow is modeled as a homogeneous two-phase mixture composed of a liquid part and a vapor part. Because the vapor density is several orders of magnitude smaller than the liquid density, the contribution of the gas phase to the overall momentum and mass conservation is neglected. Under this assumption, the homogeneous density, ρ, can be expressed as the product of the liquid density and the local liquid volumetric fraction f_L:

$$\rho \approx f_L \rho_L. \tag{2.1}$$

The parameter f_L represents the fraction of liquid volume within a computational cell, that is, the ratio between the local liquid volume and the total control-volume size. Its value therefore ranges between 0 and 1. To avoid numerical singularities, however, a lower threshold of f_L is imposed, because the vapor density is neglected.. In the present formulation the variable is constrained within the interval

$$0.1 \leq f_L \leq 1.0. \tag{2.2}$$

When $f_L = 1.0$, the control volume is completely filled with liquid, whereas values close to $f_L = 0.1$ indicate a predominantly vapor-filled region.

2.1.1 Mass Conservation

The evolution of the liquid fraction and the associated mass conservation are governed by the continuity equation:

$$\frac{\partial(f_L \rho_L)}{\partial t} + \frac{\partial(f_L \rho_L u_i)}{\partial x_i} = 0, \tag{2.3}$$

where u_i denotes the velocity component in the i-th direction. This equation expresses the conservation of the liquid mass within each control volume, accounting for both density fluctuations and changes in the liquid volume fraction due to phase change.

To linearize the equation and simplify its implementation in a weakly compressible formulation, the liquid density ρ_L is decomposed into a reference value and a small perturbation:

$$\rho_L = 1 + \rho'_L, \qquad |\rho'_L| \ll 1. \tag{2.4}$$

Under isentropic conditions, the low Mach number approximation relates the temporal variation of density to that of pressure:

$$\frac{D\rho'_L}{Dt} = M^2 \frac{Dp}{Dt}, \tag{2.5}$$

where $M = u_\infty / c_{sound}$ is the reference Mach number and in this case c_{sound} is the speed of sound in the liquid. Substituting this relation into the mass conservation equation gives the evolution of the liquid volume fraction:

$$\frac{Df_L}{Dt} + f_L \left(M^2 \frac{Dp}{Dt} + \frac{\partial u_i}{\partial x_i} \right) = 0. \tag{2.6}$$

Eq. ((2.6)) shows that the variation of f_L depends on the compressibility term, which scales with M^2, and on the divergence of the velocity field, which represents the volumetric expansion or contraction of the flow. Since the Mach number is fixed across the computational domain, it acts as a controlling parameter for the strength of the compressibility effects in the liquid phase.

2.1.2 Momentum Conservation

The motion of the liquid phase is governed by the non dimentionalized momentum conservation, expressed as

$$\frac{\partial(f_L \rho_L u_i)}{\partial t} + \frac{\partial(f_L \rho_L u_i u_j)}{\partial x_j} = -\frac{\partial p}{\partial x_i} + \frac{\partial(f_L \tau_{ij})}{\partial x_j}, \tag{2.7}$$

where p is the pressure and τ_{ij} the viscous stress tensor. After simplifying it and dividing by f_L, the momentum equation takes the following final form:

$$\frac{\partial u_i}{\partial t} + u_j \frac{\partial u_i}{\partial x_j} = -\frac{1}{f_L}\frac{\partial p}{\partial x_i} + \frac{\partial \tau_{ij}}{\partial x_j}. \tag{2.8}$$

Eq. (2.8) governs the time evolution of the velocity field of the fluid, and, together with the continuity equation (2.6), defines the fundamental dynamics of the liquid phase. The viscous stress tensor for a Newtonian fluid is defined as

$$\tau_{ij} = \frac{1}{Re}\left(\frac{\partial u_i}{\partial x_j} + \frac{\partial u_j}{\partial x_i} - \frac{2}{3}\,\delta_{ij}\,\frac{\partial u_k}{\partial x_k}\right), \tag{2.9}$$

where $Re = cu_\infty/\nu_L$ is the Reynolds number, with ν_L representing the kinematic viscosity of the liquid. The divergence of the viscous tensor can be expanded as

$$\frac{\partial \tau_{ij}}{\partial x_j} = \frac{1}{Re}\left(\frac{\partial^2 u_i}{\partial x_j \partial x_j} + \frac{1}{3}\frac{\partial}{\partial x_i}\frac{\partial u_k}{\partial x_k}\right). \tag{2.10}$$

The second term in parentheses corresponds to the contribution of bulk viscosity and becomes negligible when the velocity field is nearly divergence free, an assumption valid for the low Mach number regime considered in this study. Thus, the expression is simplified into

$$\frac{\partial \tau_{ij}}{\partial x_j} \simeq \frac{1}{Re}\frac{\partial^2 u_i}{\partial x_j \partial x_j}. \tag{2.11}$$

Eq. ((2.6)), ((2.8)), and ((2.11)) together form the governing system used in the present numerical framework. This formulation captures the essential physics of weakly compressible cavitating flows. It provides the basis for the subsequent implementation of the cavitation model described in the following sections.

2.2 SGS model

The space-filtered mass conservation equation and equation of motion are expressed as:

$$\frac{Df_L}{Dt} + f_L\left(M^2\frac{D\bar{p}}{Dt} + \frac{\partial \bar{u}_i}{\partial x_i}\right) = 0, \tag{2.12}$$

$$\frac{\partial \bar{u}_i}{\partial t} + \bar{u}_j\frac{\partial \bar{u}_i}{\partial x_j} = -\frac{1}{f_L}\frac{\partial}{\partial x_j}\left(\bar{p} + \frac{2}{3}f_L k_{SGS}\right) + \frac{\partial}{\partial x_j}\left[2\left(\nu_{SGS} + \frac{1}{Re}\right)\bar{S}_{ij}\right], \tag{2.13}$$

Where $\bar{S}_{ij}$ represents the rate-of-strain tensor. The one-equation dynamic model is used as the SGS model, giving the SGS kinetic energy k_{SGS} and the SGS kinematic eddy-viscosity coefficient ν_{SGS}. In this model, the ν_{SGS} is obtained by

$$\nu_{SGS} = C_\nu \Delta_\nu \sqrt{k_{SGS}} \tag{2.14}$$

Where C_ν=0.05 is the non-dimensional constant and Δ_ν the dimension of the computational grid.[42]
k_{SGS} derives from solving the transport equation:

$$\frac{\partial k_{SGS}}{\partial t} + \bar{u}_i \frac{\partial k_{SGS}}{\partial x_j} = -\tau_{ij}\bar{S}_{ij} - C_\varepsilon \frac{k_{SGS}^{3/2}}{\bar{\Delta}} - \varepsilon_w + \frac{\partial}{\partial x_j}\left[(C_d \Delta_\nu \sqrt{k_{SGS}} + \nu)\frac{\partial k_{SGS}}{\partial x_j}\right] \tag{2.15}$$

The production term in Eq. 2.15, which indicates the energy transfer from GS to SGS portion of turbulence kinetic energy, is evaluated by dynamic procedure of Germano et al.[26] and Lilly[43]. k_{SGS} reaches automatically the value of zero in the laminar region and is also zero on the solid wall due to the boundary condition [44].

2.3 Baseline cavitation model

The baseline cavitation model is based on the homogeneous fluid model developed by Okita & Kajishima [45]. The source term used is:

$$\frac{Df_L}{Dt} = [C_g(1 - f_L) + C_l f_L](\bar{p} - p_v) \tag{2.16}$$

where the saturated vapor pressure p_v, is found through the cavitation number, σ. Cavitation number is a non-dimensional number, essential in fluid dynamics to evaluate the cavitation phenomena. It is expressed as follow:

$$\sigma = \frac{p_\infty - p_v}{\frac{1}{2}\rho u_\infty^2} \tag{2.17}$$

The values of model constants C_g and C_l are those used for a cavitation flow around a square cylinder [45], they are set to:

- C_g=1000 and C_l=1 for $\bar{p} < p_v$
- C_g=100 and C_l=1 for $\bar{p} > p_v$.

2.4 PDF-based model

The limitation of the conventional SGS models is that the SGS vortices are modeled by eddy viscosity so the local low-pressure region cannot be considered, meaning the related cavity generation is ignored. To address this limitation, Singhal et al.[22] introduced a new cavitation model. The main innovation of the model lies in the assumption that phase change rates (evaporation and condensation) depend not only on the local Reynolds-averaged pressure but also on pressure fluctuations from the average. The instantaneous pressure can drop below the vapor pressure even if the mean pressure remains above it. To quantify this, the model employs a PDF to account for the probability of the pressure in a computational cell. In Singhal's formulation, a top-hat PDF (top-right image of Fig.2.1) was used to link the phase change rates to the turbulent kinetic energy (k), where the pressure fluctuations are estimated as $p' = 0.39\rho k$. Following this approach, the idea has been further extended to LES frameworks. In this context, the PDF is used to represent the spatial pressure distribution within a computational cell. By introducing the PDF into LES, it becomes possible to account for the cavitation induced by unresolved small-scale structures, effectively modeling the SGS cavitation inception that would otherwise be missed by the filtered pressure field.

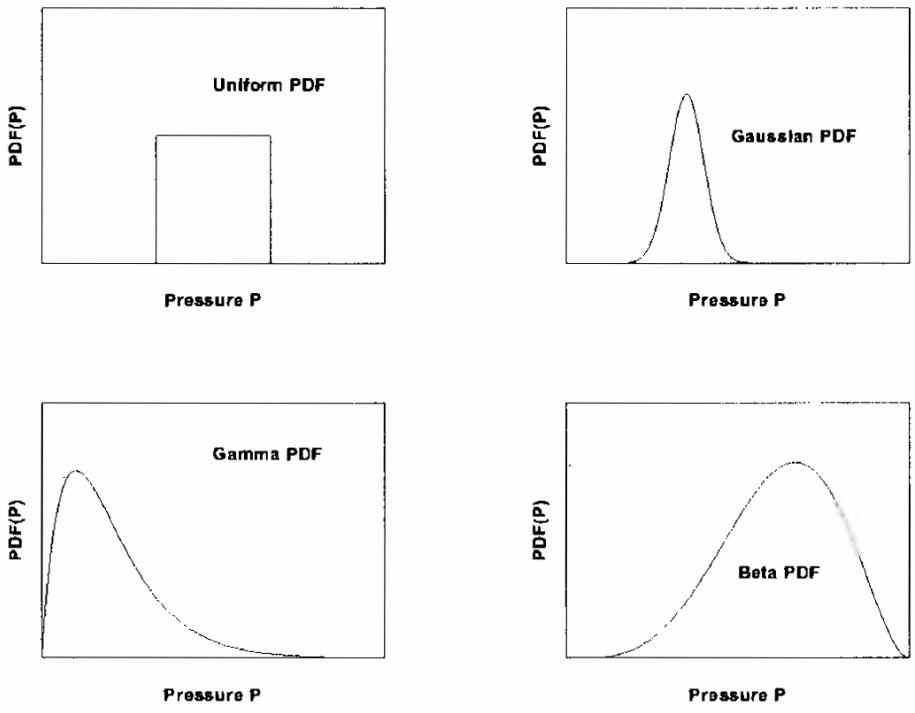

Figure 2.1: Various forms of PDF

In the new model formulation, the PDF is implemented with the use of a Gaussian distribution as shown in Fig.2.2 [4]. This distribution might be more accurate than a top hat one based on the assumption that, when considering a random variable falling within a particular range, larger differences in values are less likely to occur than smaller ones.

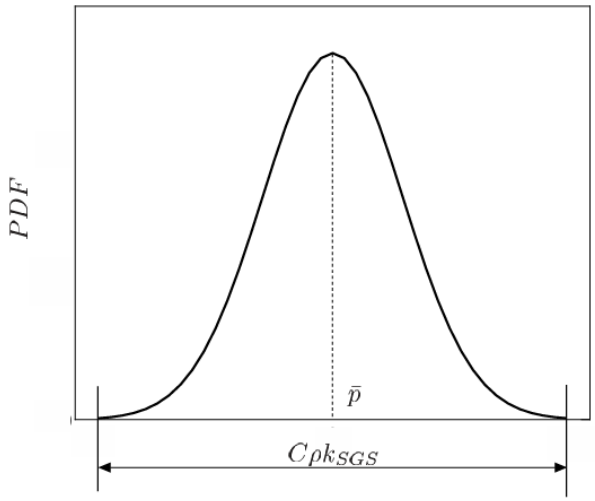

Figure 2.2: Basic concept of Gaussian pressure distribution

The model Eq. (2.16) is thus changed into:

$$\frac{Df_L}{Dt} = \int_{-\infty}^{\infty} [C_g(1-f_L) + C_l f_L](p-p_v)\psi(p)dp \tag{2.18}$$

The PDF $\psi(p)$ is the Gaussian distribution function that uses the filtered pressure $\bar{p}$ as the mean value.

$$\psi(p) = \frac{1}{\sqrt{2\pi}s}\exp\left[-\frac{(p-\bar{p})^2}{2s^2}\right] \tag{2.19}$$

The variable s stands for the standard deviation of the pressure.
When considering a Gaussian PDF, the range between the mean value of the parameter taken into consideration plus/minus three times the standard deviation of such variable ($\bar{p} \pm 3s$) contains 99.7% of the probability of finding the value of the parameter in such interval. Thus in Eq. (2.18) the extremes of integration are modified into:

$$\frac{Df_L}{Dt} = [C_g(1-f_L) + C_l f_L] \int_{\bar{p}-3s}^{\bar{p}+3s} (p-p_v)\frac{1}{\sqrt{2\pi}s}\exp\left[\frac{(p-\bar{p})^2}{2s^2}\right] dp \tag{2.20}$$

Similarly to the correlation between pressure fluctuations and turbulent kinetic energy observed in single-phase turbulent flows, inspired from the statistical theory

of homogeneous isotropic turbulence [46], the relationship between the pressure variation p_{SGS} in a computational cell and the subgrid-scale turbulence energy in the present case assumes to be expressed as:

$$p_{SGS} = C\rho k_{SGS} \tag{2.21}$$

Since the characteristic amplitude is $6s$, the typical scale of the sub-grid scale pressure fluctuations can also be written as:

$$p_{SGS} = 6s \tag{2.22}$$

By combining Eq. (2.21) and (2.22) together, the correlation between p_{SGS} and k_{SGS} is expressed as:

$$s = \frac{C}{6}\rho k_{SGS} \tag{2.23}$$

The validity of Eq. (2.21) were investigated using DNS data of turbulent mixing layer [47]. The constant C was also determined. In the study, filtering operations were applied to a DNS database of a single-phase turbulent mixing layer in order to formulate the low-pressure regions of the subgrid scale (SGS) that could serve as potential sources of cavity formation. The analysis revealed that both the SGS pressure fluctuations and the turbulent energy are predominantly distributed within the shear layers, where the motion of turbulent vortices is most pronounced.
In regions where the turbulent energy is sufficiently developed, a strong correlation between these two quantities was identified. On the contrary, other areas where p_{SGS} is low display a weak correlation, however those areas are not significant for the occurrence of cavitation. The proportionality constant linking ρk_{SGS} and p_{SGS} in the shear layer was found to be of the order of 10^0, more accurately around 3-5, allowing for the estimation of nearly the entire pressure fluctuation across the flow field using this single parameter [4]. Furthermore, it was demonstrated that the instantaneous pressure distribution within a computational cell could be approximated using the estimated SGS pressure fluctuations together with a Gaussian distribution based on the filtered mean pressure from fine-scale vortical structures [4]. These findings suggested that, if unsteady turbulence at scales larger than those resolved by LES can be adequately captured, and the corresponding SGS turbulent energy estimated, it becomes possible to predict the initiation of cavitation arising.
In this specific application, there are three possible situations that can be found, as represented by Fig. 2.3.

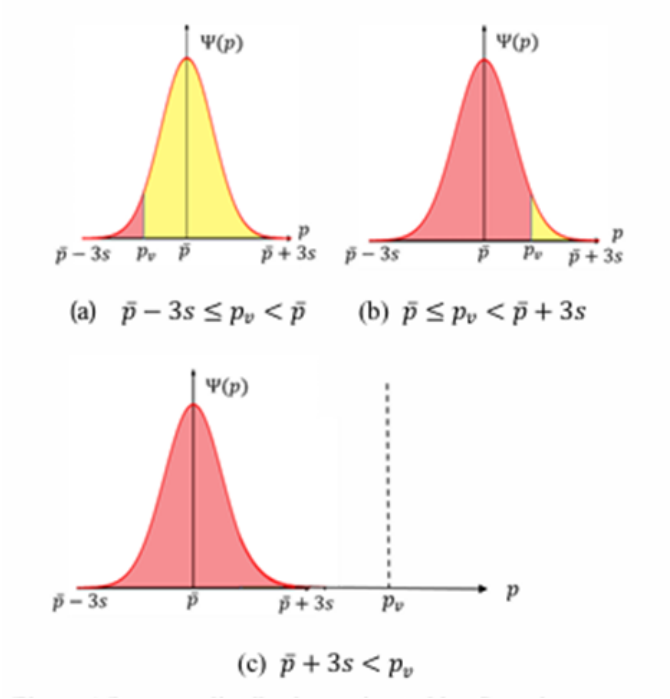

Figure 2.3: Gaussian distribution

The important difference between the three configurations shown is the relationship between the mean pressure value $\bar{p}$ (which is the pressure value assigned to the cell considered, when the PDF model is not applied) and the liquid vapor pressure p_v (which is the value for which the fluid transit from liquid to gaseous). In the previous model the only case taken into account for the generation of cavity in the SGS was when $\bar{p} < p_v$.
Now, the three possible situations are:

- **Situation (a):** In this case, $(\bar{p} - 3s) < p_v < \bar{p}$. Since cavitation occurs only when $p < p_v$, the integration interval of Eq. (2.20) is, in this case, limited between $\bar{p} - 3s$ and p_v. The right side of the curve(yellow part) is ignored because it does not lead to cavity generation but, on the contrary, if considered in the integration interval, would lead to cavity disappearance because in that side the pressure is higher than p_v.

- **Situation (b):** In this case, $\bar{p} < p_v < \bar{p} + 3s$. For this configuration the the baseline cavitation model assign to the cell the pressure value of $\bar{p}$, which is lower than p_v thus the generation of cavitation for that cell is considered even without the use of the PDF Model. The application of the PDF model for those kind of cells, on the contrary, would lead to cavity generation only for

the red area, where $p < p_v$ so it would lead to less cavity generation. That's why for this study it is best to maintain the baseline cavitation model.

- **Situation (c):** Similarly to case (b), when $p_v > \bar{p} + 3s$, there is no necessity to apply the PDF Model because also the standard LES Model accounts for the cavitation generated in the cell.

To summarize, the only moment when the PDF Model is necessary is when $(\bar{p} - 3s) < p_v < \bar{p}$ which is why the integration source term, Eq. (2.20), is modified into:

$$\frac{Df_L}{Dt} = [C_g(1 - f_L) + C_l f_L] \int_{\bar{p}-3s}^{p_v} (p - p_v) \frac{1}{\sqrt{2\pi}s} \exp[\frac{(p - \bar{p})^2}{2s^2}] dp \tag{2.24}$$

2.5 Numerical scheme

The numerical method for unsteady flows is based on the fractional step method for incompressible flows with the collocated arrangement of the variables.

$$u_i^* = u_i^{(n)} + \frac{\Delta t}{2}[3F_i^{(n)} - F_i^{(n-1)}], \tag{2.25}$$

where n represents the number of time step and Δt is the time increment.
The second order Adams—Bashforth method is applied to the convection and viscous terms, are represented by F_i. The velocity of the next step is obtained by adding the gradient of updated pressure to the fractional step velocity as:

$$u_i^{(n+1)} = u_i^* - \Delta t \frac{1}{f_L^{(n)}} \delta_i (\bar{p}^{(n+1)} + \frac{2}{3} f_L^{(n)} k_{SGS}^{(n+1)}) \tag{2.26}$$

Here, δ_i means the second-order central difference. The pressure equation is discretized as follow by using the three -step method (second order accuracy) for the time difference and the central difference for the spatial difference.

$$\frac{Df_L}{Dt} + f_L^{(n)} \Bigg\{ M^2 \left(\frac{3p^{(n+1)} - 4p^{(n)} + p^{(n-1)}}{2\Delta t} + u_j^{(n)} \delta_j p^{(n+1)} \right) + f_L^{(n)} \delta_j u_j^* \\ - f_L^{(n)} \Delta t \, \delta_j \left[\frac{1}{f_L^{(n)}} \delta_j \left(p^{(n+1)} + \frac{2}{3} f_L^{(n)} k_{SGS}^{(n+1)} \right) \right] \Bigg\} = 0 \tag{2.27}$$

The pressure equation is solved with the relaxation method. Note that the equation is an Helmholtz type equation and is diagonally dominant, so sufficient

convergence can be ensured. The Jacobi method, which is also suitable for calculations on vector computers, is used for the convergence calculation. When the Mach number is zero and f_L is constant, it reduces to the Poisson equation for the pressure of a normal incompressible flow [4].
The time progression for the liquid volumetric fraction f_L is performed semi-implicitly in two stages. First an explicit prediction is made as follows:

$$f_L^P = f_L^{(n)} + \Delta t\{C_g(1-f_L) + C_l f_L\}^{(n)}(p^{(n+1)} - p_v) \tag{2.28}$$

If $f_L^P \leq 1$ and $f_L^{P'} < 1$ when $f_L^{(n)} < 1$ (with $f_L^{(P')}$ being a temporal extrapolation of f_L, for instance $f_L^{(P')} = 3f_L^{(n)} - f_L^{(n-1)} + f_L^{(n-2)}$), cavity is expected to exist in the cell at the next time step. Using the pressure $p^{(n+1)}$, the updated f_L of the first stage can be obtained as:

$$f_L^* = f_L^{(n)} + \Delta t\{C_g(1-f_L) + C_l f_L\}^{(n)}(p^{(n+1)} - p_v) \tag{2.29}$$

If $f_L^P \geq 1$ then $f_L^* = 1$:

$$f_L^{(n+1)} = f_L^* - \Delta t u_j^{(n+1)} \delta_j f_L^* \tag{2.30}$$

Note that in this calculation, as mentioned before, for the gas phase density, a lower limit is set to $f_{L\min} = 0.1$ to prevent the interlocking amount within the cell from becoming zero. In previous calculations [4], it has been confirmed that the time when $f_L \leq 0.1$ is sufficiently short, and the number of cells where $f_L = 0.1$ is also sufficiently small that they can be ignored.
By the above procedure, the flow field at the new time step $p^{(n+1)}$, $u_i^{(n+1)}$, $f_L^{(n+1)}$ are obtained and by repeating this process, the unsteady flow, including the phase change due to cavitation, is calculated [1].

2.6 Computational setup and target of analysis

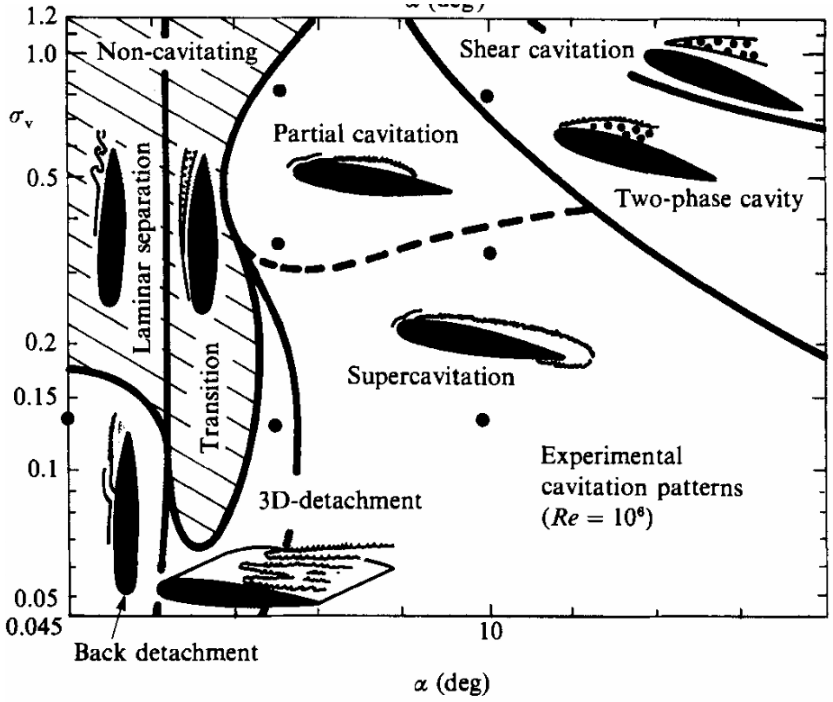

Figure 2.4: Behaviour of cavitation

As is shown in Fig. 2.4[48], when considering a hydrofoil profile, the appearance of cavitating phenomena is deeply linked to the conditions on which the profile is found. Two key factors that determine the behavior of cavitation are: the angle of attack at which the profile is found (α) and the cavitation number of the flow (σ). A high σ value means that there is a good margin between the local pressure and the vapor pressure (p_v), so the probability of cavitation is low. On the other hand, a lower σ means that cavitation phenomena are more likely to occur.
In this research, the attention is focused on a Clark–Y 11.7% profile under two operating conditions, selected to investigate different cavitation and flow regimes. The first condition corresponds to an angle of attack of $\alpha = 8°$ and a cavitation number $\sigma = 1.2$, which are conditions where unsteady sheet cloud cavitation occurs, leading to lift breakdown. In this configuration, under single-phase flow conditions, laminar separation and subsequent reattachment occur. In many homogeneous fluid models, lift breakdown arises from σ values greater than 1.2 because these models underestimate the sheet cavity length. The purpose of this setup is therefore to investigate the effect of cavitation initiation from subgrid-scale (SGS) vortices on the sheet cavity length. For this operating conditions, a considerable amount

of data is available from both Computational Fluid Dynamics (CFD) analyses, such as RANS [21], DES [40], and LES [22], and experimental measurements [49], [50], [51], [52]. The second condition is characterized by an angle of attack of $\alpha = 20°$ and $\sigma = 2.7$. At $\alpha = 20°$, turbulent separation occurs over most of the hydrofoil under single-phase conditions, making the effects of shear flow and turbulent vortices significant. Moreover, the condition $\alpha = 20°$, $\sigma = 2.7$ has corresponding experimental data[49],[52], which were selected for comparison.

The computational domain and boundary conditions of the profile are summarized in Fig. 2.5. For the velocity field, a no-slip condition is applied at the hydrofoil surface, a zero-gradient condition is imposed at the upper and lower boundaries, and a periodic condition is used in the spanwise direction. For the pressure field, a non-reflective boundary condition is applied at the inflow, outflow, and lower far-field boundaries, while a periodic condition is also applied in the spanwise direction. This last approximation can be made because the experimental data show that the cavity is almost homogeneous in the span-wise direction [1].

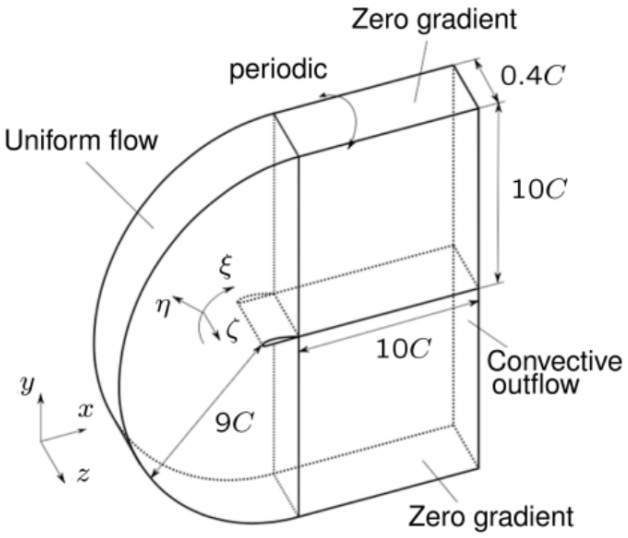

Figure 2.5: Boundary conditions [1]

A C-type body-fitted mesh was chosen to solve the boundary layer around the hydrofoil. The grid counts 512, 200 and 100 points in the ξ-, η-, and ζ- directions respectively.

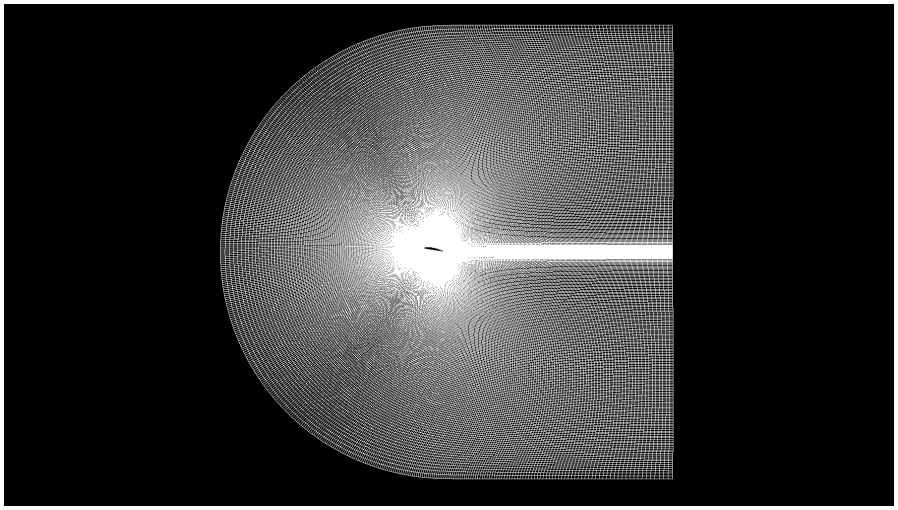

Figure 2.6: Mesh

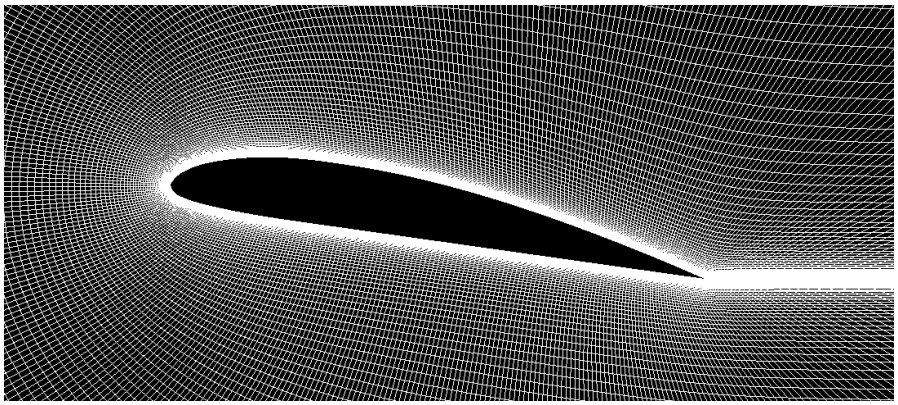

Figure 2.7: Mesh around the profile

The wall-normal width of the first grid is $5 \times 10^{-5}c$, equivalent to less than 2 in the wall unit of the single-phase condition. The flow considered is water at 13°C and the flow conditions for the two cases are summarized in Table 2.1:

Table 2.1: Flow parameters for the two profiles.

Parameter	Case 1	Case 2
Chord length, c [mm]	77.0	77.0
Spanwise length	$0.4c$	$0.4c$
Angle of attack, α [°]	8	20
Cavitating number, σ	1.2	2.7
Velocity [m/s]	11.0	11.0
Mach number, M	7.6×10^{-3}	7.6×10^{-3}
Reynolds number,Re	6.41×10^{5}	6.41×10^{5}

2.7 Domain decomposition for post-processing

In order to analyze the results obtained, through Fortran coding, the computational domain is divided into a grid with $n_x = 512$, $n_y = 200$, and $n_z = 100$ nodes.

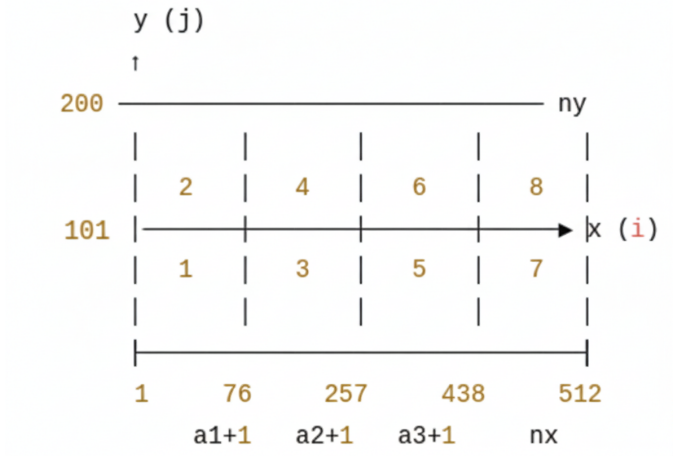

Figure 2.8: Domain division

The horizontal division along the $x-$direction is organized into four segments, with partition points at $a_1 = 75$, $a_2 = 256$, and $a_3 = 437$. Along the $y-$direction, two bands are defined: one ranging from 1 to 100 and the other from 101 to 200. Consequently, the horizontal domain is subdivided into eight blocks in total.
In the $z-$direction, each block includes the total of all 100 cells. Thus, while all

blocks have the same extent of 100 grid points along the $y-$axis, their size along the $x-$axis varies: blocks 1, 2, 7, and 8 have a length of 75 cells, whereas the central blocks have a length of 181 cells. Volume integration was performed within each region. This division will be used when studying the behavior of parameters such as the cavity volume generated or the turbulent kinetic energy (k_{SGS}) in specific areas like the Leading Edge and the Trailing Edge.

Chapter 3

Results and discussion for Case 1

For this study, the analysis has been carried out for three configurations depending on whether the PDF model is applied or not and on which value of the model constant C is used:

- **First configuration** : PDF Model with $C = 5$,
- **Second configuration** : PDF Model with $C = 10$,
- **Third configuration**: Without PDF implementation.

The goal of this analysis is to determine whether the PDF model is able to account for the cavity generation caused by the SGS pressure fluctuations effectively and, if so, to identify which model constant is more suitable for a more accurate simulation.

3.1 Cell Volume

To assess whether the implementation of the PDF model improves cavity generation, the total cavity volume is evaluated for the three situations described in Fig. 2.3. Figs. 3.1, and 3.2 show the cavity volume generated within the computational domain for the $C = 5$ and $C = 10$, respectively.

The y-axis represents the sum of volumes corresponding to the cells shown in Fig. 2.4(a)-(c). From the graphs, it is evident that even though the probability of Situation (a) (when $p - 3s < p_v < \bar{p}$) is relatively low compared to the other two situations, its contribution to the total cavitation volume is significant, leading to an important increase of cavity formation.
This result confirms that the PDF model applied to the SGS vortices influences

cavity generation, effectively increasing cavitation within the SGS.
Indeed, without the PDF model this contribution would be zero(blue curve, corresponding to Situation (a)), and the SGS cavitation would be limited to the yellow and orange curves (Situations (b) and (c)).
As expected, by comparing the cavity volume for the two model parameters, it becomes clear that the PDF model with a higher constant ($C = 10$) produces a larger generated volume for Situation (a)(blue curve), which is consistent with the fact that a higher model constant increases the standard deviation of the Gaussian probability distribution. Consequently, a wider range of pressure values satisfies the condition $\bar{p} - 3s < p < p_v$.

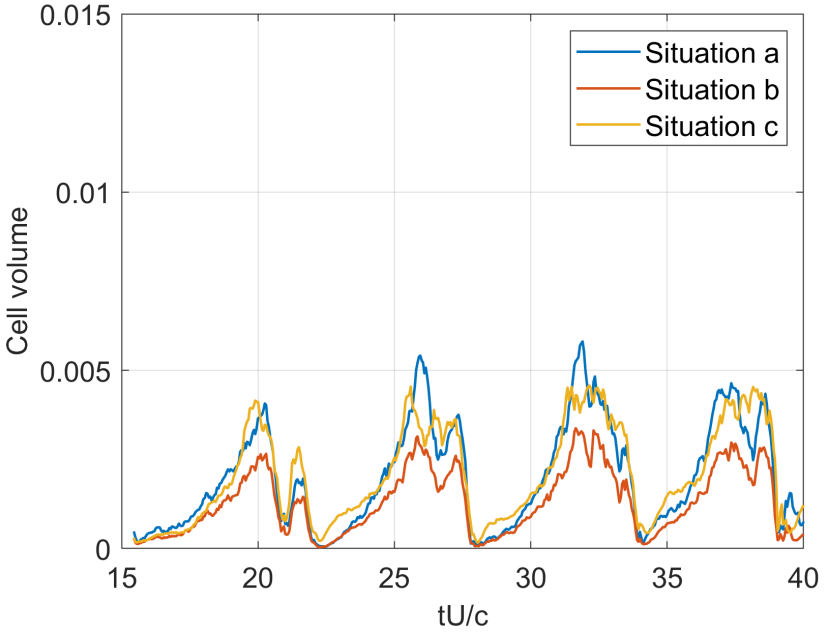

Figure 3.1: Cavity generation for $C = 5$.

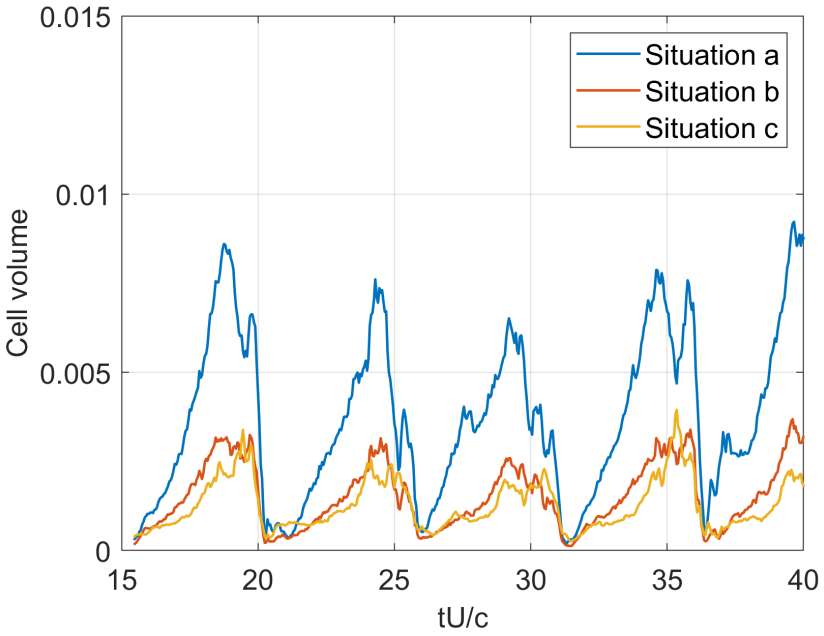

Figure 3.2: Cavity generation for $C = 10$.

The trend mentioned above can also be confirmed by visual inspection of the cavitation patterns around the hydrofoil at a given time step. In Figs. 3.3 and 3.4, the coexistence of two types of cavity generation can be observed: in red, the cavitation corresponding to Situation (b); in green, the cavitation associated with Situation (a). Both situations exhibit comparable magnitudes.(Situation (c) would be analog)

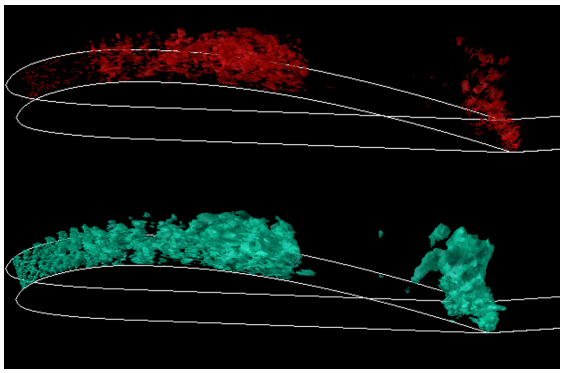

Figure 3.3: Cavity generation at a given time step for $C = 5$.

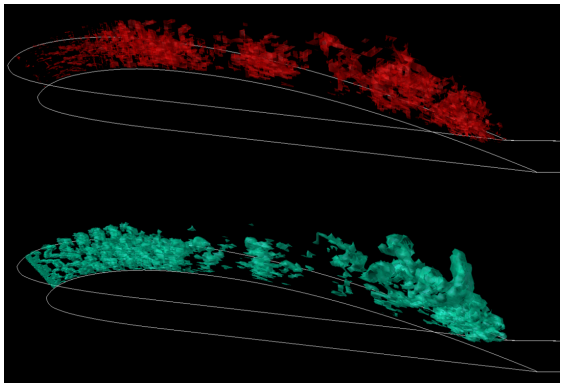

Figure 3.4: Cavity generation at a given time step for $C = 10$.

3.2 Pressure Distribution

Regarding the pressure distribution, previous CFD analyses were unable to reproduce the experimental pressure coefficient profiles (c_p) accurately. Figure 3.5, taken from Okabayashi et al. [1], compares the pressure profiles obtained from experiments conducted at Kyushu University [53] with those from CFD analyses using different turbulence models, including RANS, DES, and LES [54],[55]. The results show that none of these CFD approaches successfully replicate the experimental behavior of the pressure distribution. In particular, at the leading edge, the experiments reveal a clear flat region between $0c$ and $0.25c$, which is not observed in the numerical simulations. This means that the CFD analysis are unable to simulate the minimum sheet cavity length properly [1]. Furthermore, moving towards the trailing edge, the experimental $-C_p$ decreases more gradually than in the CFD results, indicating that cavitation persists longer in the experiment.

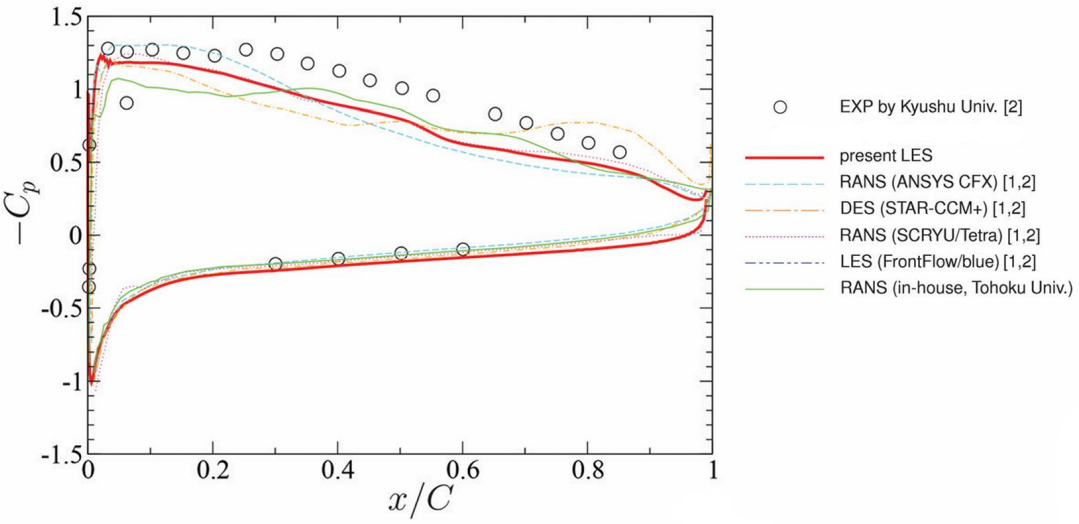

Figure 3.5: Comparison between experimental and CFD pressure distributions, adapted from [1].

Regardless of the value of the model constant C, Fig. 3.6 shows that no significant improvement is observed when compared with the LES model without the PDF approach. A slight improvement can, however, be noticed near the leading edge, where the PDF models produce a short flat region between $0c$ and $0.15c$ that none of the other CFD methods captured. This feature is closer to the experimental data and suggests that the PDF approach may help improve the prediction of the minimum cavity length. Overall, this result makes the c_p distribution obtained

with the PDF model slightly more consistent with experimental observations but not satisfactorily.

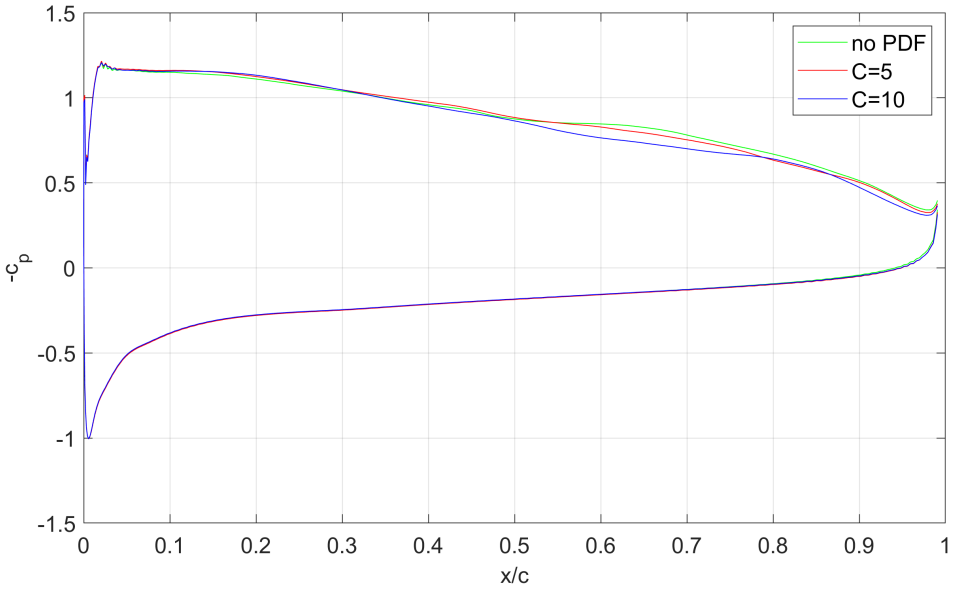

Figure 3.6: Pressure coefficient distribution for the different models.

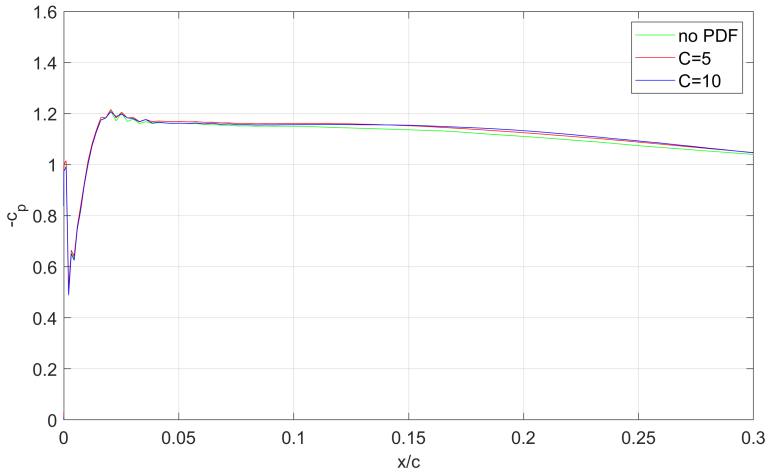

Figure 3.7: Zoomed view near the leading edge.

3.3 Lift and Drag Distribution

Two other essential performance parameters analyzed are the lift and drag coefficients (C_L and C_D). Figures 3.8, 3.9, and 3.10 show the temporal evolution of these coefficients for the three cases. The three cases produce similar, though not identical, trends. Ignoring the initial transient iterations, both lift and drag coefficients generally exhibit a quasi-periodic behavior. The case with $C = 5$ shows noticeable instabilities around $tu_\infty/c = 28$ and $tu_\infty/c = 39$ for both C_L and C_D. This is due to the pressure waves non-periodically generated by cavity collapse. The mean values of C_L and C_D do not show significant improvement compared with previous CFD models. The C_L values are nearly identical to those obtained without the PDF model, and a similar trend is observed for C_D. This lack of improvement indicates a limitation of the current model, which fails to enhance the prediction of the time-averaged coefficients. However, although the mean values are similar, the temporal variations of the coefficients differ: the PDF models exhibit more pronounced peaks and fluctuations, especially the $C = 5$ case, as can be seen by the RMS values of the fluctuations listed in Table 3.1. This behavior is associated with the stronger cavity generation and instabilities observed in these cases.

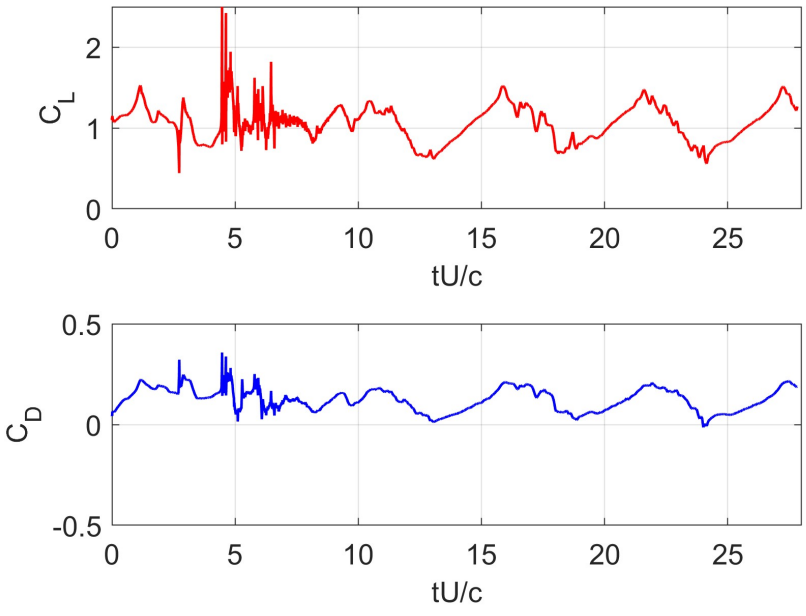

Figure 3.8: Lift and drag coefficients for the case without the PDF model.

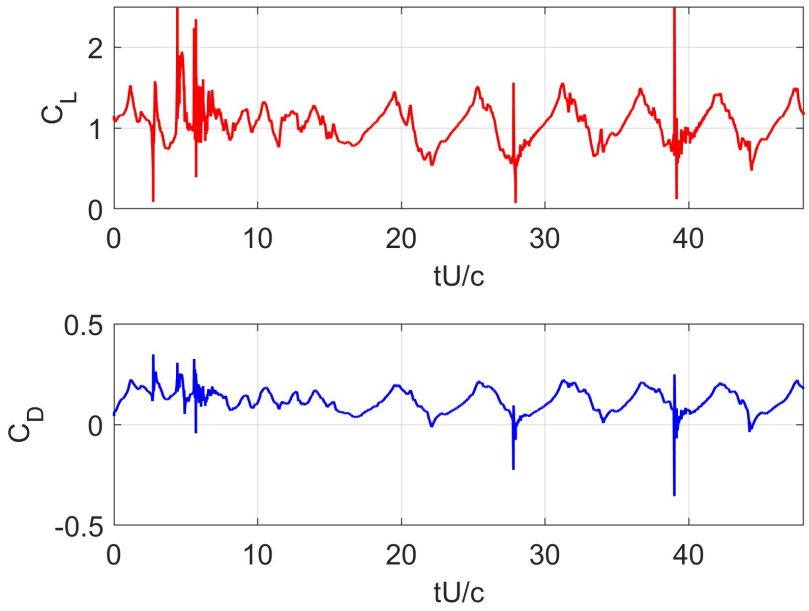

Figure 3.9: Lift and drag coefficients for the PDF model with $C = 5$.

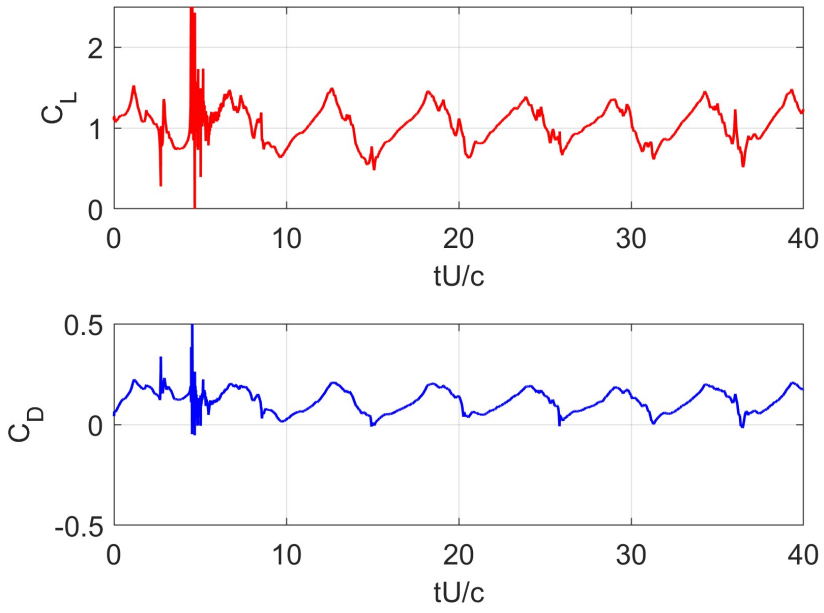

Figure 3.10: Lift and drag coefficients for the PDF model with $C = 10$.

Table 3.1: Mean values of C_L and C_D for the three models

Case	$\boldsymbol{C_L}$	$\boldsymbol{C_D}$	$\boldsymbol{RMS}$ **%**
No PDF	1.045	0.115	20.1
PDF $C = 5$	1.028	0.113	23.3
PDF $C = 10$	1.026	0.109	21.7

To gain a deeper understanding of the coefficient behavior, a Fast Fourier Transform (FFT) analysis was performed. The FFT provides information about the theoretical periodicity, dominant frequency, and Strouhal number for each case (Table 3.2). The Fast Fourier Transform (FFT) is a numerical algorithm that converts a time-domain signal into its frequency-domain representation, providing information about the amplitude and phase of the signal [56]. In fluid dynamics, it enables the identification of dominant oscillation frequencies associated with vortex shedding and unsteady aerodynamic or hydrodynamic forces [57].

The lift coefficient C_L was analyzed over the stationary portion of the signal(for instance for the $C = 5$ case the interval selected was $15 \leq tu_\infty/c \leq 48$). Before applying the FFT, the mean value of the signal was removed and a Hann window was applied to reduce spectral leakage. The single-sided amplitude spectrum was computed and normalized as

$$P_1(f) = \frac{2}{N} |\hat{C}_L(f)|,$$

where N is the number of samples and $\hat{c}_L(f)$ is the Fourier transform of the windowed signal. The dominant frequency f_{dom} was identified as the maximum of $P_1(f)$, yielding the theoretical period and Strouhal number:

$$T_{\text{FFT}} = \frac{1}{f_{\text{dom}}}, \qquad St = \frac{f_{\text{dom}}\, c}{u_\infty}.$$

To visualize the main oscillation, the signal was filtered around the dominant frequency ($\Delta f = \pm 0.005$ Hz) and reconstructed via inverse FFT; the average period was also independently estimated from peak detection in the filtered signal, and the spectrum was validated using Welch's PSD method.

In particular, the Strouhal number ($St = fc/u_\infty$) characterizes the relationship between the dominant oscillation frequency and the characteristic flow velocity and length. In hydrofoil and bluff-body flows, it provides a dimensionless measure of vortex shedding and unsteady force oscillations [58, 59]. Spectral analysis via FFT often reveals a clear dominant frequency that, when expressed through the Strouhal number, enables comparison between flow regimes and the identification

of periodic flow instabilities [60, 61, 62], as can be seen in Figs.3.11, 3.12 and 3.13. The values of the Strouhal number are expressed in Table 3.2 obtained in this analysis are consistent with those measured in Watanabe's experiments [50]. The non-dimensional periodicity slightly decreases in the PDF models, especially for $C = 10$, indicating a higher frequency of cavitation events, again in agreement with experimental observations.

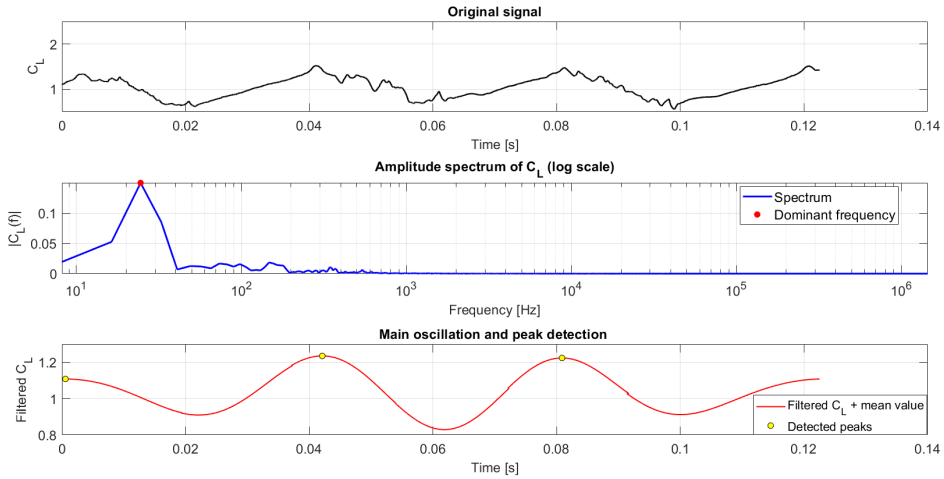

Figure 3.11: FFT spectrum for the No-PDF model.

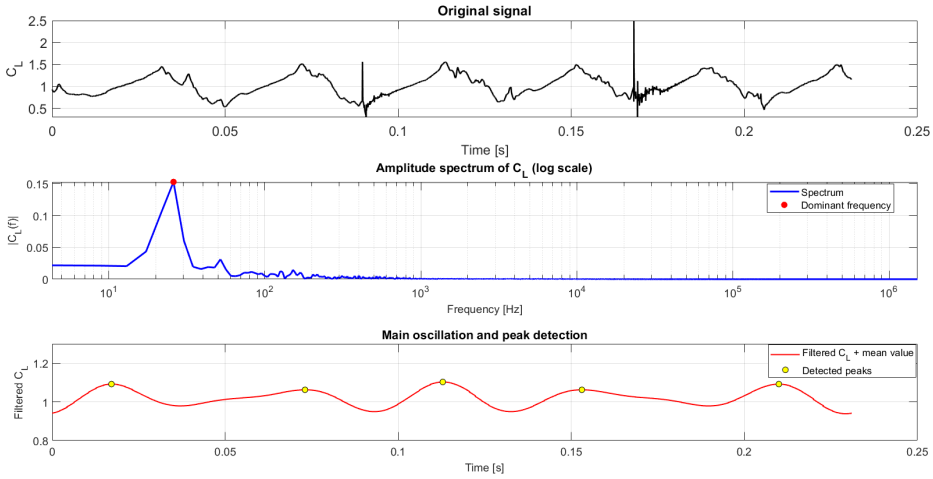

Figure 3.12: FFT spectrum for the PDF model with $C = 5$.

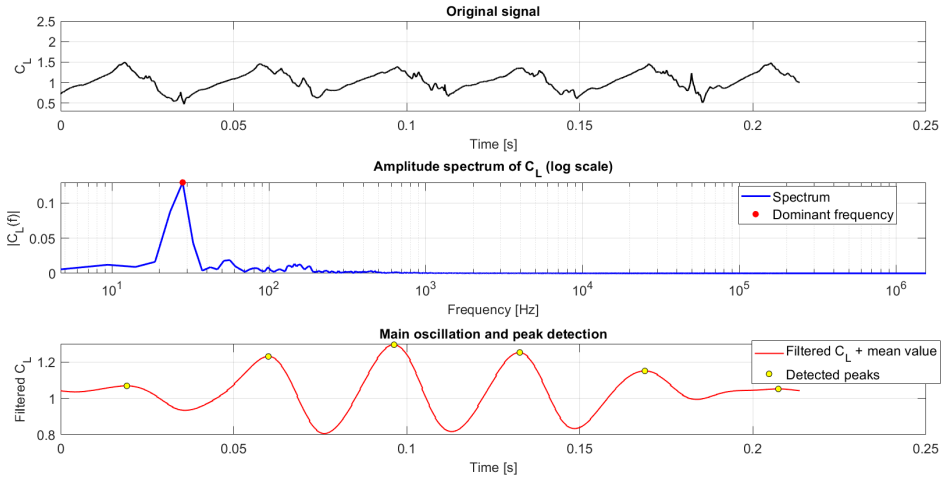

Figure 3.13: FFT spectrum for the PDF model with $C = 10$.

Figs. 3.11, 3.12, 3.13 show the lift coefficient C_L, the amplitude spectrum of C_L as a function of frequency, and the reconstructed main oscillation for each analyzed case. Especially from the third graph of each figure, it is clear that the PDF model results exhibit less periodic trends, likely due to their ability to better capture the strong instability of the phenomenon. Table 3.2 reports the dominant frequency, corresponding period, non-dimensional periodicity, and Strouhal number for each model.

Table 3.2: Parameters of the FFT analysis

Case	**Dominant Frequency [Hz]**	**Theoretical Periodicity[s]**	**Adimensional Periodicity**	**Strouhal Number**
No PDF	24.04	0.042	6	0.168
PDF C=5	25.51	0.039	5.57	0.179
PDF C=10	28.10	0.036	5.14	0.196
Watanabe Exp.	-	-	-	0.18

As mentioned before, the periodicity decreases for the PDF models due to the increase of the dominant frequency. This is an important result, a higher dominant frequency indicates that cavitating structures tend to form and detach more frequently, confirming that these models predict a more unsteady and dynamic flow behavior. A notable difference in frequency, and thus periodicity, also emerges

between the two PDF cases: the $C = 10$ model shows higher frequencies and thus faster cycles of cavity growth and collapse compared to $C = 5$. Comparison with the experimental results suggests that the more accurate prediction is probably obtained with $C = 5$, as its non-dimensional periodicity and Strouhal number are closer to the experimental results found by Watanabe [50], where the Strouhal number is around 0.18. As for the dominant frequency, Watanabe calculated the values for when $\sigma = 1.46$ and when $\sigma = 0.90$ finding, respectively, $f_{dom} = 50\ Hz$ and $f_{dom} = 9\ Hz$, making it plausible for the dominant frequency to reach values around $25 - 28\ Hz$ when $\sigma = 1.2$. Figures 3.14, 3.15 and 3.16 display the behavior of a cycle of cavitation and the corresponding C_L values at each step and the related non-dimensional time. C_L slowly increase while the sheet cavity begins and grow along the profile, reaching the peak values when the sheet cavity reaches the maximum elongation. After that, the cavitation rapidly changes shape into bubbles that concentrates in the Trailing Edge area and then detaches from it and disappear. Comparing the no PDF cycle with the other two, it is quite clear that the first case doesn't show as much cavity generation as the other two cycles, especially when the sheet cavity is fully developed. Also, regarding the cycles found from the two PDF models, a slight difference can be noted. In Fig. 3.16, which corresponds to C=10, a long sheet cavity that covers almost all the profile is sustained for a longer time compared to the cavity behavior for the PDF C=5 case. In addition, the decrease of C_L, on average, is less smooth and presents rapid changes.
This conduct is again coherent with the higher C value and the consequently smaller periodicity. The cause of the generated peaks is the collapse of the cavity and bubble disappearance.

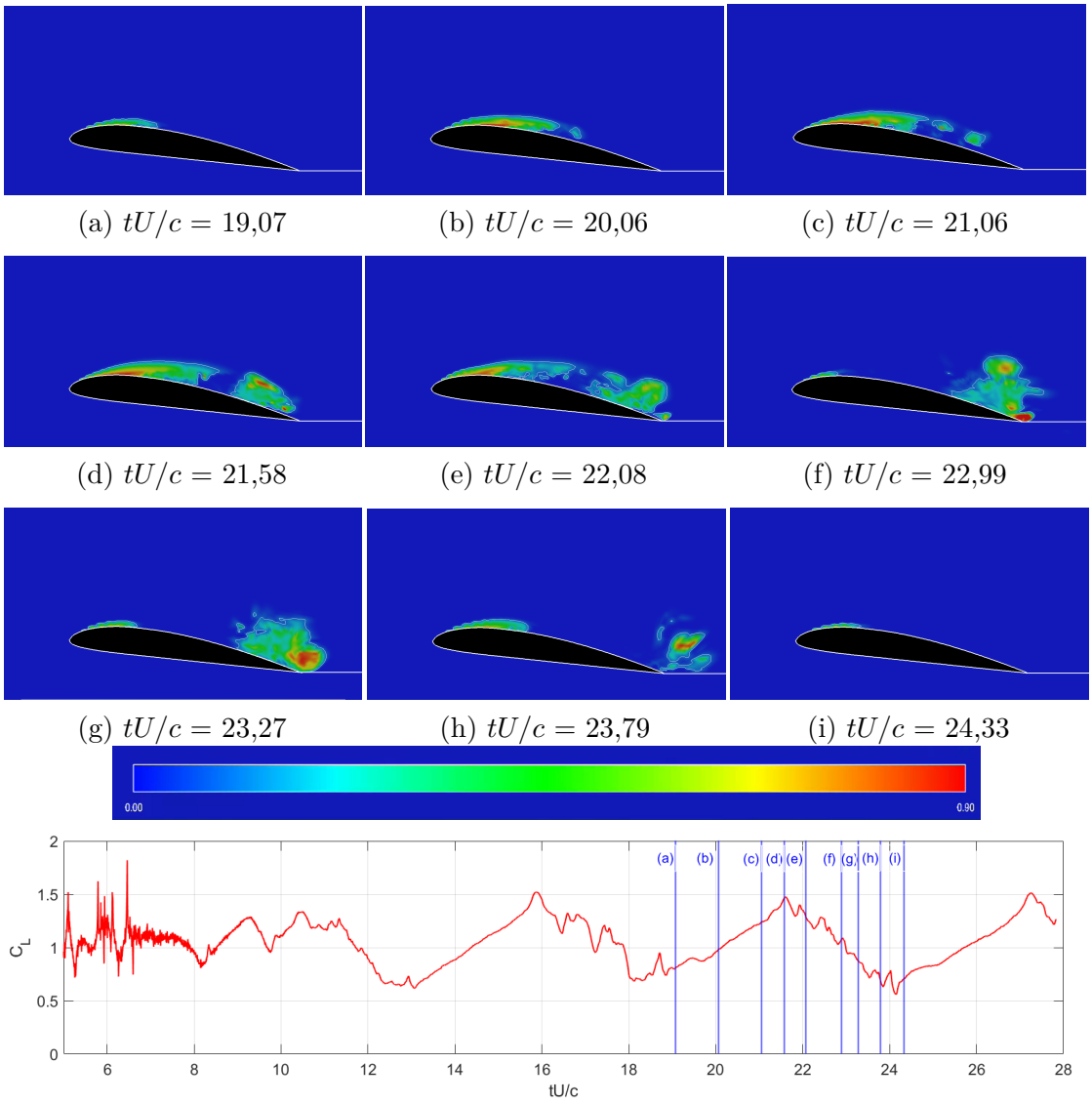

(a) $tU/c = 19{,}07$ (b) $tU/c = 20{,}06$ (c) $tU/c = 21{,}06$

(d) $tU/c = 21{,}58$ (e) $tU/c = 22{,}08$ (f) $tU/c = 22{,}99$

(g) $tU/c = 23{,}27$ (h) $tU/c = 23{,}79$ (i) $tU/c = 24{,}33$

Figure 3.14: Cavity cycle for No-PDF case

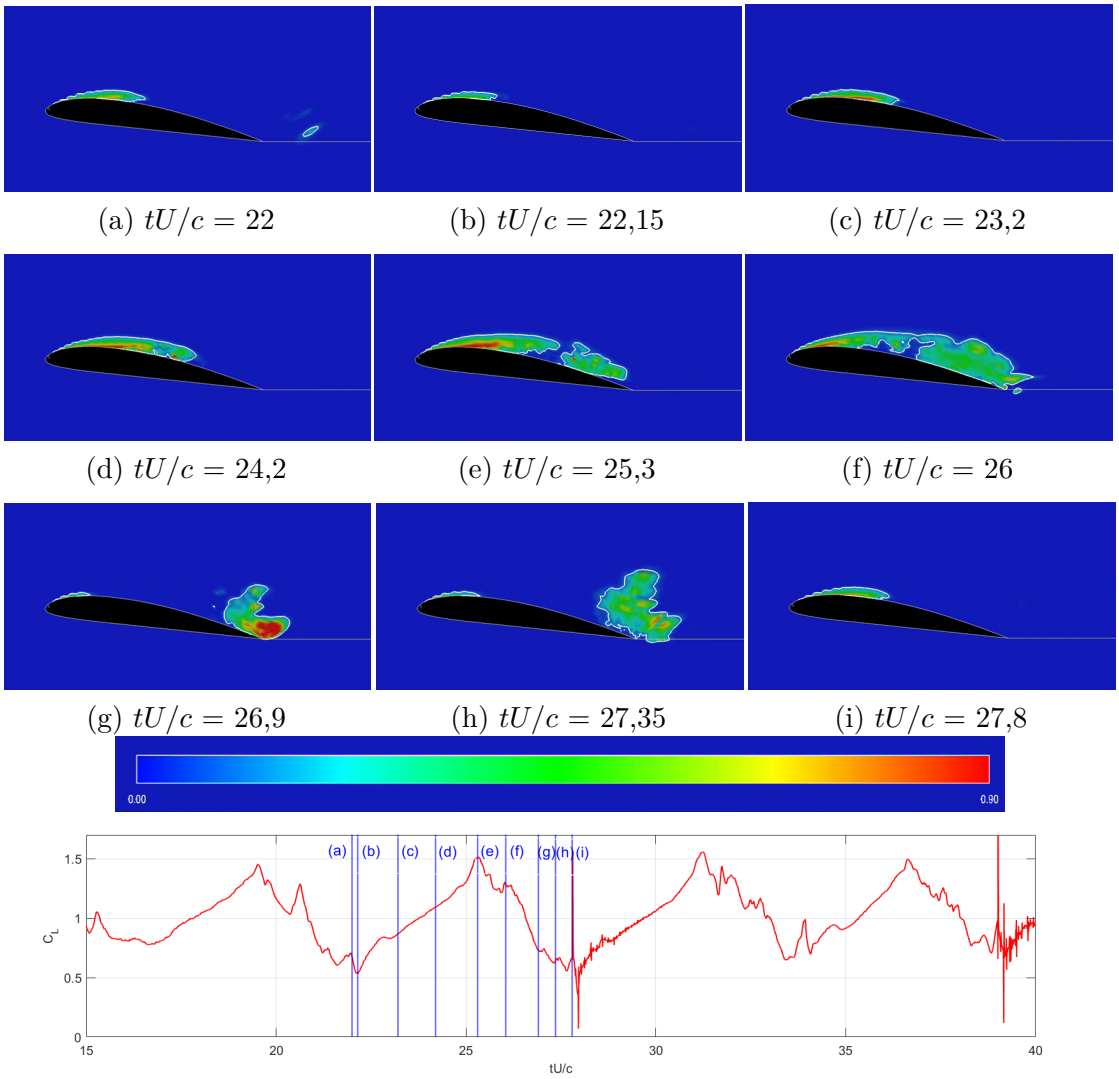

(a) $tU/c = 22$ (b) $tU/c = 22{,}15$ (c) $tU/c = 23{,}2$

(d) $tU/c = 24{,}2$ (e) $tU/c = 25{,}3$ (f) $tU/c = 26$

(g) $tU/c = 26{,}9$ (h) $tU/c = 27{,}35$ (i) $tU/c = 27{,}8$

Figure 3.15: Cavitation cycle and C_L value for C=5 case

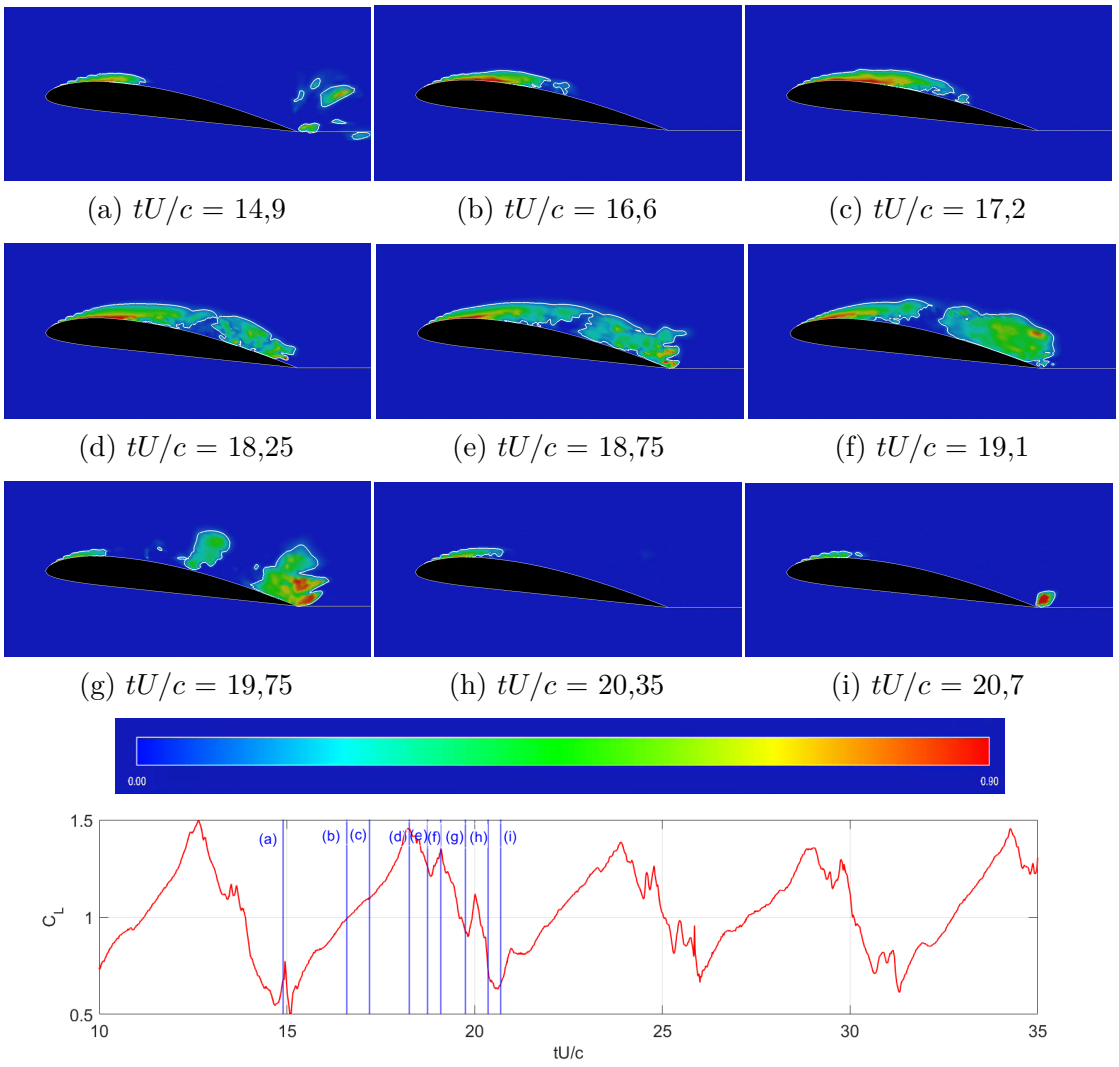

(a) $tU/c = 14{,}9$ (b) $tU/c = 16{,}6$ (c) $tU/c = 17{,}2$

(d) $tU/c = 18{,}25$ (e) $tU/c = 18{,}75$ (f) $tU/c = 19{,}1$

(g) $tU/c = 19{,}75$ (h) $tU/c = 20{,}35$ (i) $tU/c = 20{,}7$

Figure 3.16: Cavitation cycle and C_L value for C=10 case

3.4 Turbulent Energy formation

In the visualizations of Fig. 3.17 and 3.18, the distribution of the SGS kinetic energy and the isoline corresponding to a liquid volume fraction of $f_L = 0.1$, which represents approximately 90% vapor content, are shown. Through these images, a complete cycle of cavitation dynamics can be observed, consisting of the formation and development of a sheet cavity, followed by the generation, growth, and detachment of a cloud cavity. Once the main vapor structure separates from the attached sheet cavity, secondary bubbles form downstream as a result of the local pressure depression induced by the main cavity itself. Additional bubble-type cavities are also produced near the trailing edge, where strong vortical structures promote local pressure reductions.
Regions of high SGS turbulent kinetic energy are concentrated around the cavity interfaces, where intense pressure gradients are present, particularly in the vicinity of the re-entrant jet area. These localized peaks of SGS kinetic energy highlight the strong coupling between the resolved flow field, the unsteady cavity dynamics, and the SGS turbulence production mechanisms.
It is difficult to gasp a strong difference in the turbulence development between the two PDF models. Conversely, comparing these cavitation cycles with the ones seen in the no PDF model, a general increase in turbulence and cavity generation is clearly confirmed.

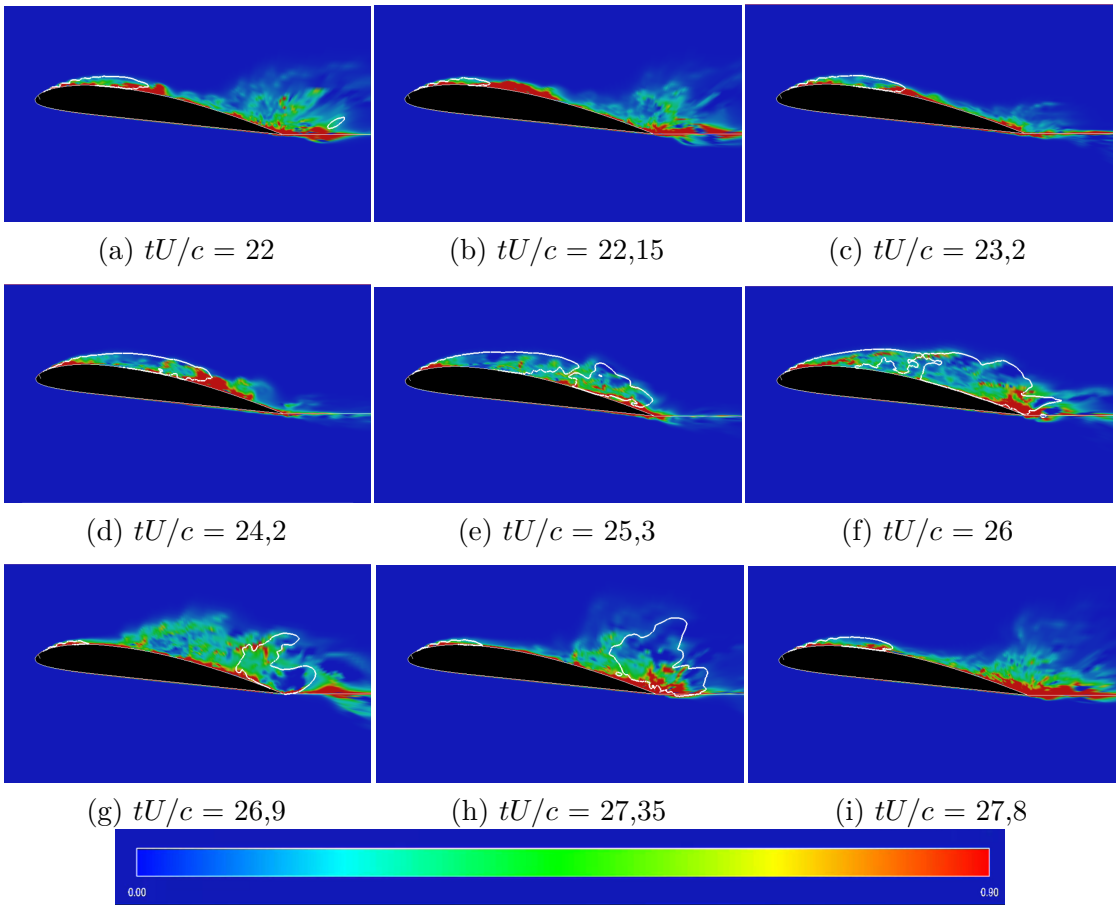

(a) $tU/c = 22$ (b) $tU/c = 22{,}15$ (c) $tU/c = 23{,}2$

(d) $tU/c = 24{,}2$ (e) $tU/c = 25{,}3$ (f) $tU/c = 26$

(g) $tU/c = 26{,}9$ (h) $tU/c = 27{,}35$ (i) $tU/c = 27{,}8$

Figure 3.17: Cavity and SGS turbulent kinetic energy for C=5 case and ($z/C = 0.2$)

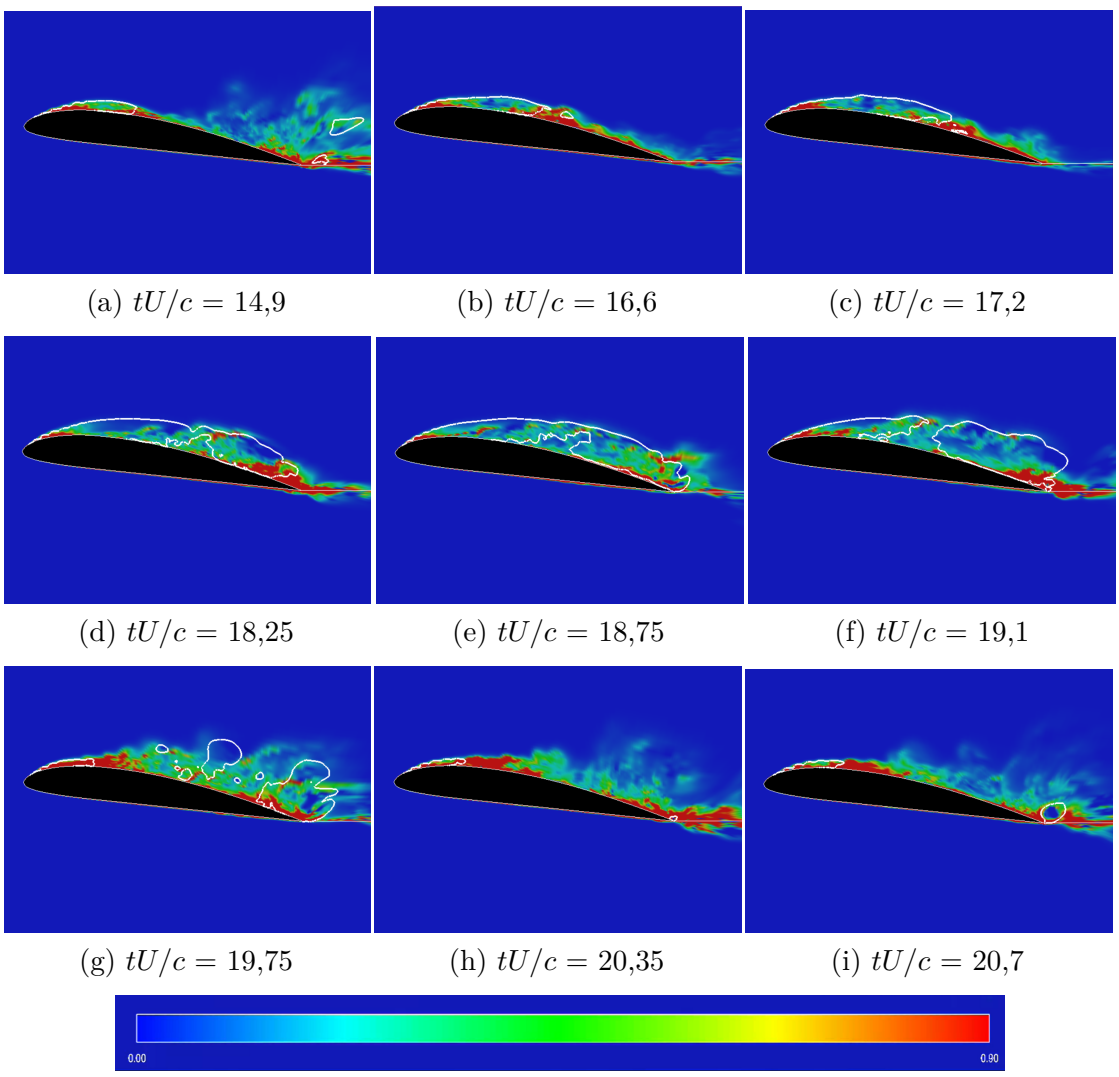

(a) $tU/c = 14{,}9$ (b) $tU/c = 16{,}6$ (c) $tU/c = 17{,}2$

(d) $tU/c = 18{,}25$ (e) $tU/c = 18{,}75$ (f) $tU/c = 19{,}1$

(g) $tU/c = 19{,}75$ (h) $tU/c = 20{,}35$ (i) $tU/c = 20{,}7$

Figure 3.18: Cavity and SGS turbulent kinetic energy for C=10 case and ($z/C = 0.2$)

3.5 Sheet Cavity Length

Regarding the minimum and maximum sheet cavity lengths, important improvements can be seen. Figure 3.19 displays the maximum sheet cavity length found with the past experiments and CFD models.

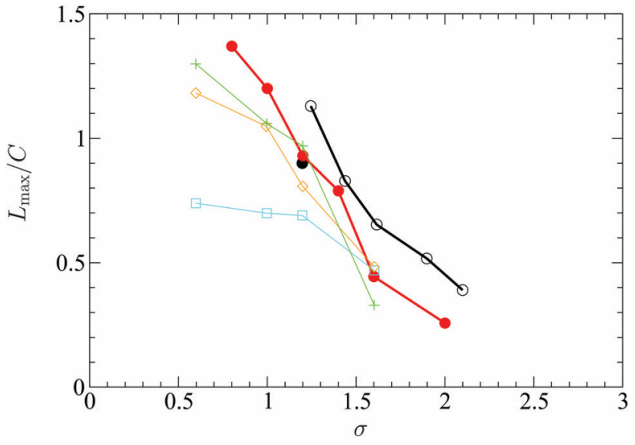

Maximum sheet cavity length (AoA = 8 deg). Red •: present LES; black ○: EXP by Kyushu Univ. [2]; black •: EXP by Numachi et al. [37]; □: RANS (ANSYS CFX) [1,2], ◇ DES (STAR-CCM+) [1,2], +: RANS (in-house, Tohoku Univ.) [1,2].

Figure 3.19: Maximum sheet cavity length for found with various models

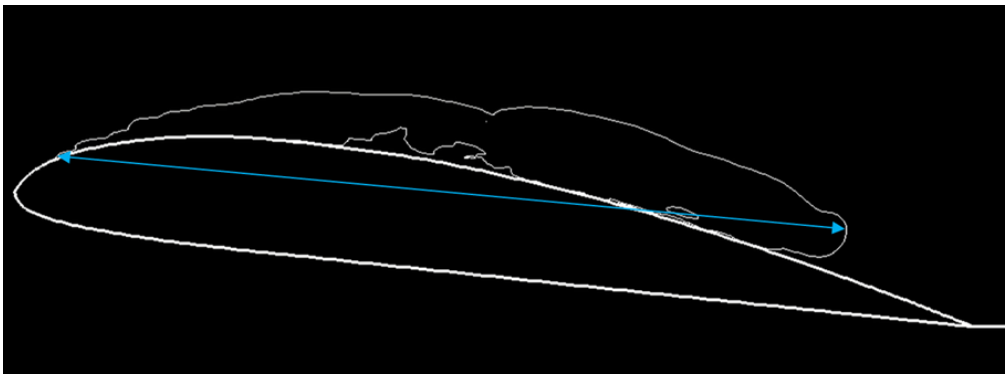

Figure 3.20: No PDF case

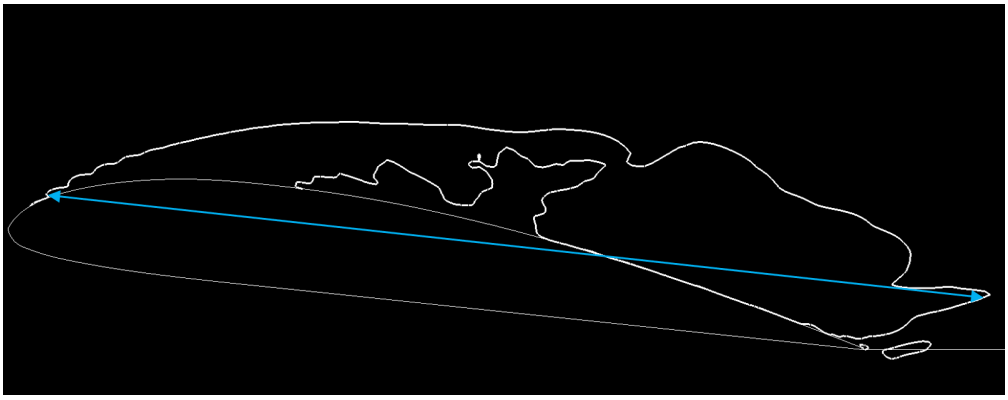

Figure 3.21: PDF C= 5 case

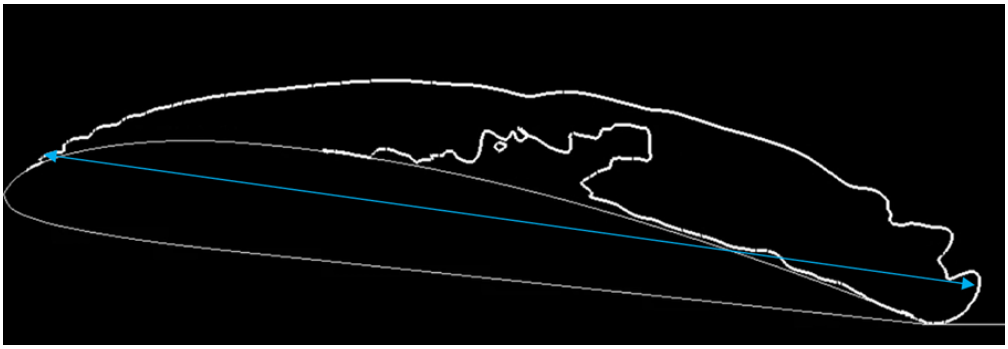

Figure 3.22: PDF C=10 case

The values reached by the PDF models show a good improvement in comparison with the past CFD models and are clearly more similar to the experimental data, for which $L_{max}/c = 1.1$ [53]. Where L_{max} stands for the maximum sheet cavity length value. As shown in Fig.s 3.17, 3.18, 3.19, while without using the PDF model, the maximum cavity length reached is smaller than the full length of the chord, with both PDF models, the chord length is reached and exceeded. On average, the minimum and maximum cavity lengths reach the following values:

Table 3.3: Relationship $L_{\max}/c$ for different PDF cases

Case	$\boldsymbol{L_{\max}/c}$	$\boldsymbol{L_{\min}/c}$
No PDF	0.82	0.0
PDF C=5	1.10	0.16
PDF C=10	1.05	0.17

This is clearly an important improvement on the sheet cavity length. Indeed, because the maximum length of the sheet cavity is bigger than the chord, then the oscillation mode can be denoted as transitional cavity oscillation, instead of simply partial cavity oscillation [4].
As it can be stated by Table 3.4[1], for an angle of attack of 8°, the condition of $\sigma = 1.2$ is a critical point in LES simulations because the current LES models are unable to properly simulate the flow conditions found in the experimental data. While experiments show that there should be a transitional cavity oscillation flow, LES simulations are only able to show a partial cavity oscillation regime. The goal of the analysis is thus to understand whether this new model can improve the simulations giving back results more similar to those found in the experiments.

Table 3.4: Behaviours of cavitation at various cavitation numbers for $\alpha = 8°$

σ (-)	Present (LES)	Watanabe et al. (EXP)
3.0	Noncavitation	Noncavitation
2.0	Steady sheet cavity	Steady sheet cavity
1.6, 1.4	Partial cavity oscillation	Partial cavity oscillation
1.2	Partial cavity oscillation	Transitional cavity oscillation
1.0, 0.8	Transitional cavity oscillation	Transitional cavity oscillation

Reaching the transitional cavity behavior, as it is displayed in the experimental results, was exactly one of the objectives of this new model. Additionally, in the new models the complete disappearance of the sheet cavity is avoided, in accordance with the experimental results. It is thus clear that the introduction of the PDF approach strongly affects the cavitation behavior around the profile.

3.6 Cell Volume at the Leading Edge

The most relevant area to analyze in this case is the Leading Edge region, where cavitation begins and develops. This region consists of the area over the first one fourth of the profile. The PDF model highlights the formation of cavity volume in this zone and clearly confirms the link between cavity generation and the turbulent SGS kinetic energy.
The cell volume associated with Situation a) provides a significant contribution to cavity formation at the Leading Edge. As expected, this region is also characterized by high values of SGS turbulent kinetic energy. Figures 3.23 and 3.24 further verify the correlation between cavity generation in Situation a) and the behavior of SGS kinetic energy: peaks of turbulent energy occur at the time steps where cavity growth is more pronounced, while low cavitation phases correspond to reduced kinetic energy. These observations support the initial hypothesis behind the PDF model, that a substantial contribution to cavitation arises from the low pressure within SGS turbulent vortices.

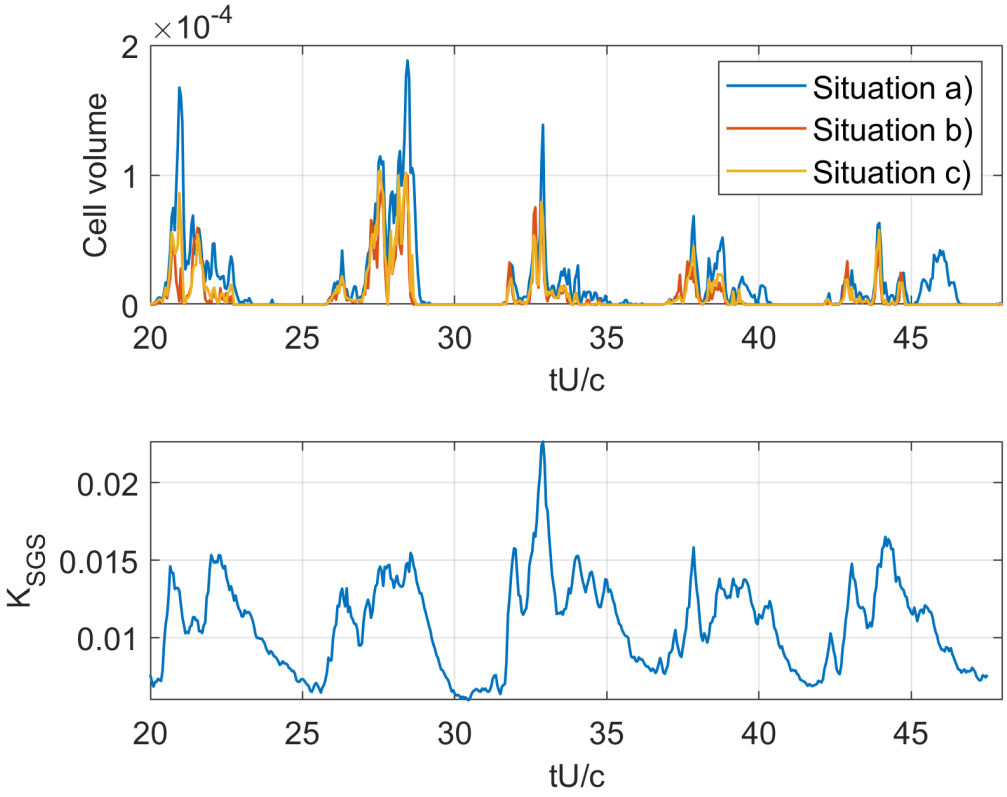

Figure 3.23: Cell Volume and K_{SGS} at the Leading Edge for the C=5 case

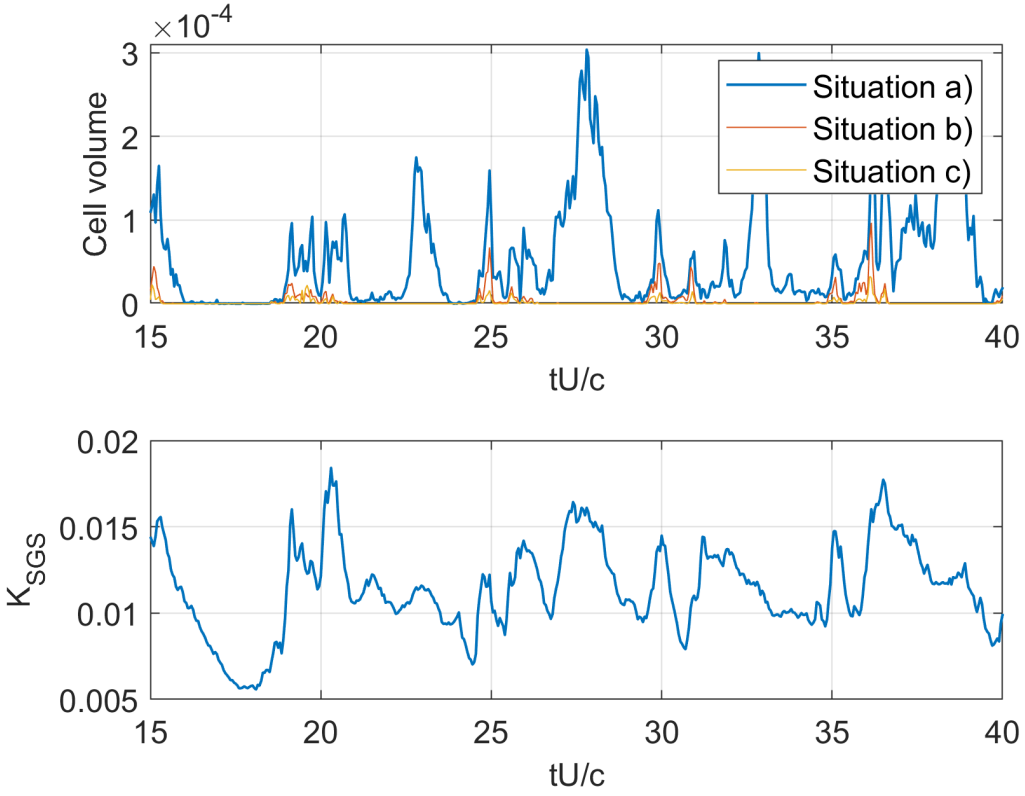

Figure 3.24: Cell Volume and K_{SGS} at the Leading Edge for the C=10 case

The correspondence between cavity generation in the SGS and the SGS turbulent kinetic energy peaks is less evident for the results of the PDF case with $C = 10$. This fact is not unexpected since k_{SGS} is directly connected with p_{SGS} trough the constant C so for higher values of C, the k_{SGS} will rise more frequently.

Chapter 4

Results and discussion for Case 2

As mentioned in the introduction, the second case analyzed consists of the same Clark-Y11.7% profile at the conditions of $\alpha = 20°$ and $\sigma = 2.7$. For this case, similar analysis were made and the results will be explained in this Chapter.
Regarding the boundary conditions, while in general, in a non cavitation condition, for an angle of attack of 8° the laminar flow detaches and reattaches near the leading edge, for α=20°, turbulence detaches over most of the wing. For this reason the focus in this case won't be the leading edge area but the trailing edge.
The stronger turbulent environment associated with this configuration leads to a more complex analysis.
For this case the comparison with the experimental results is more difficult because the heavier turbulence causes the flow to be also more affected by the different boundary condition effects such as reflection of the waves that can be generated in the experiment because of the set up.
As for the computational model, while before a time step of $\Delta t = 5 \times 10^{-6} s$ was sufficient, in this second case, the analysis required to change the time step used both for the case No PDF and for the PDF $C = 10$ one. Those two simulations indeed, when using a $\Delta t = 5 \times 10^{-6} s$ diverged. The time step was thus changed into $\Delta t = 2.5 \times 10^{-6} s$.

4.1 Cell Volume

Figures 4.1, 4.2 and 4.3 show the cell volume generation for the cases $C = 5$, $C = 10$ $\Delta t = 5 \times 10^{-6} s$ and $C = 10$, $\Delta t = 2.5 \times 10^{-6} s$. As expected, the PDF model is able to increment the cavity formation thanks to the addition of the cavity generation due to Situation a). Similarly to what was observed in *Chapter* 3, the cases where

$C = 10$, show a larger formation of cavitation due to Situation a), linked to the larger standard deviation values obtained.

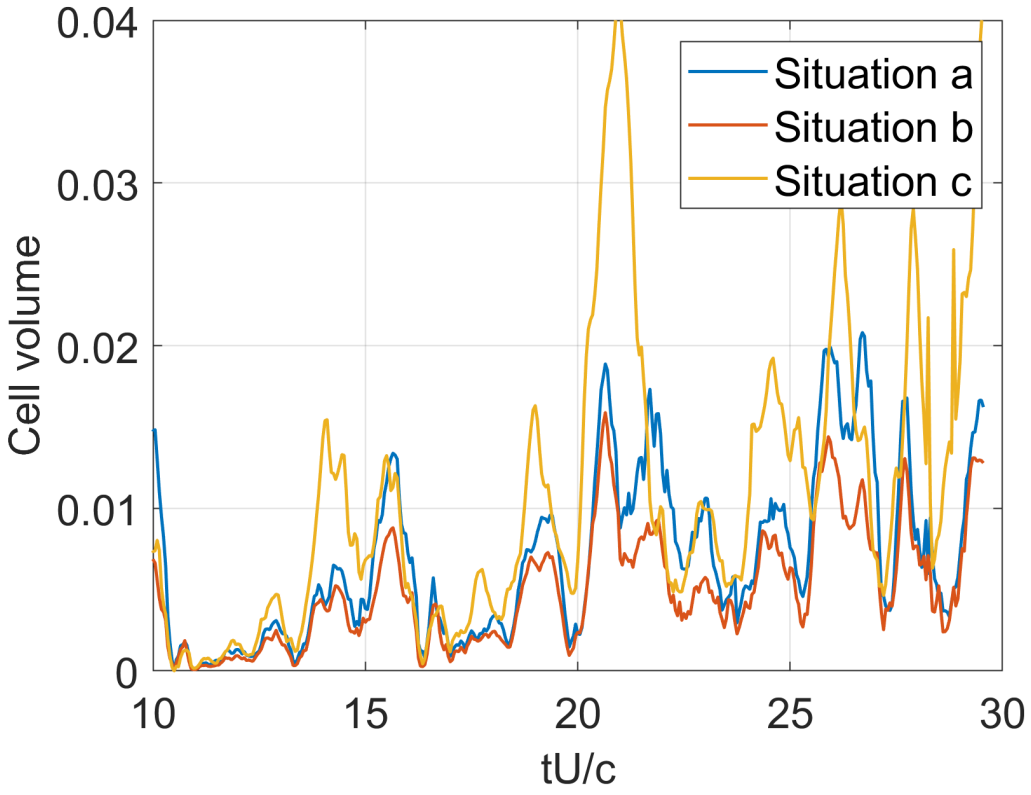

Figure 4.1: Cavity generation for $C = 5$

However, it is unexpected to see such an important difference in the values of cell volume generated due to Situation c). In that situation, the pressure in the entire cell is lower than p_v, therefore the cavitation source term is identical in the PDF and No PDF model, thus cavity generation was expected to be similar between the two models, just like it happened for the first configuration analyzed.

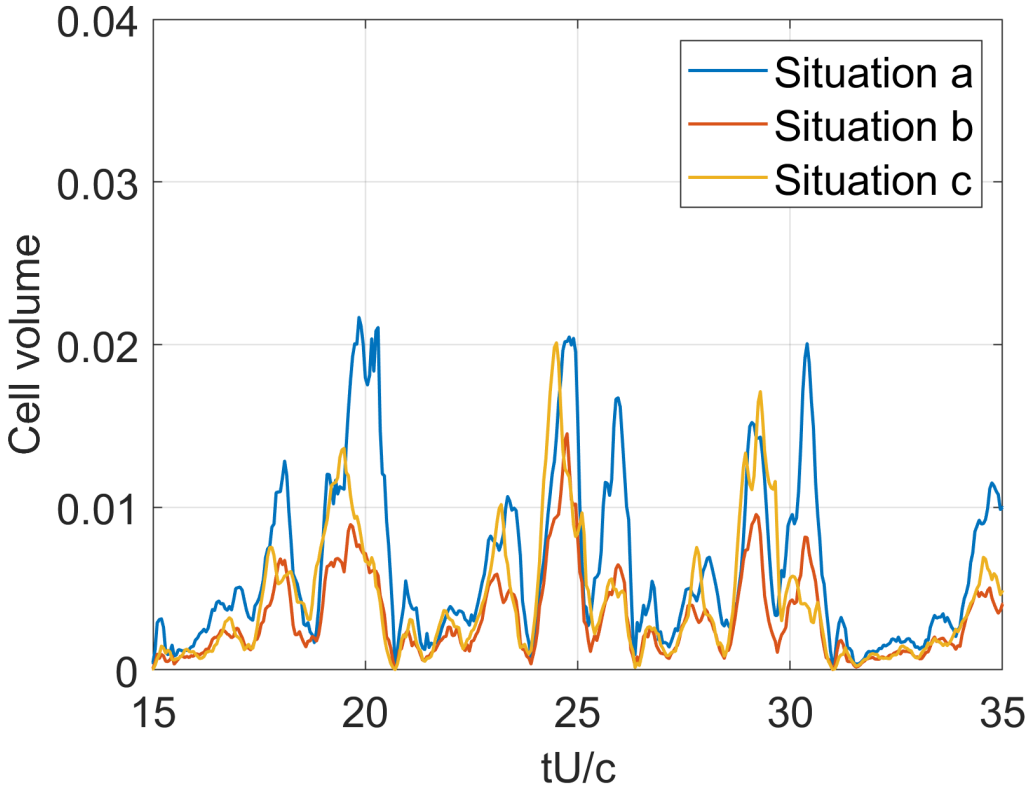

Figure 4.2: Cavity generation for $C = 10$

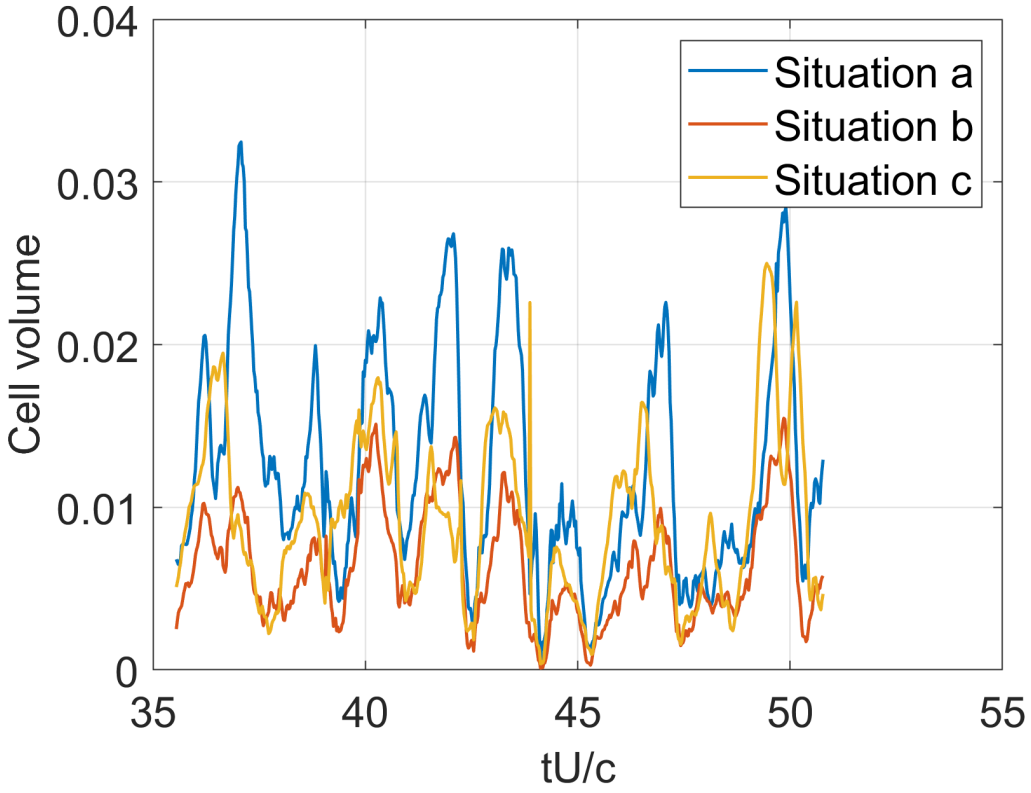

Figure 4.3: Cavity generation for $C = 10$ and $\Delta t = 2.5 \times 10^{-6} s$

4.2 Lift and Drag distribution

The behavior of the lift and drag coefficients in relation to the cavity pattern, resulting from the Kitamura et al.[49] experiments, is shown in Fig. 4.4.
Unfortunately, the model currently studied fails to show a similar behavior in the C_L and C_D coefficients. The CFD analysis, indeed, display stronger fluctuations. It is difficult to establish a clear periodicity for the coefficients even for long evaluation periods.

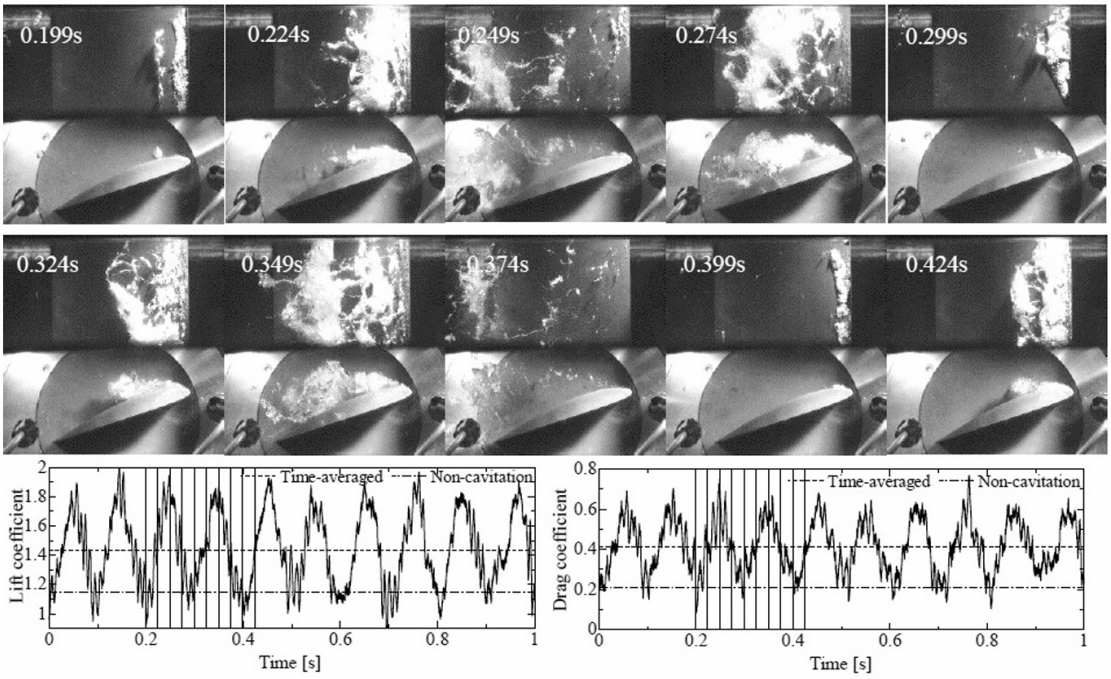

Figure 4.4: Cavity pattern of the experimental data during a few cycles of cavity oscillation $\alpha = 20°$, $\sigma = 2.7$ [49]

However, the correlation between cavity formation and coefficient pattern is in line with the correlation found in the experiments. Regardless of the inability to gasp a real periodicity in the performance coefficients, through the visualizations it is still possible to define a cavitation cycle for the No PDF and C=5 model.

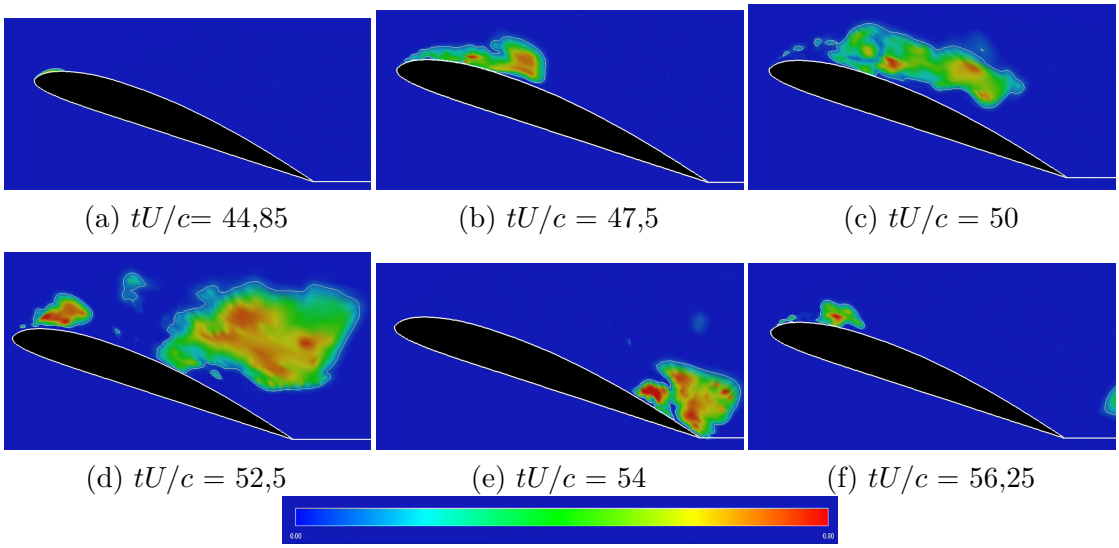

(a) tU/c= 44,85 (b) $tU/c = 47{,}5$ (c) $tU/c = 50$

(d) $tU/c = 52{,}5$ (e) $tU/c = 54$ (f) $tU/c = 56{,}25$

Figure 4.5: Cavitation cycle for the No PDF $\Delta t = 2.5 \times 10^{-6}$ case

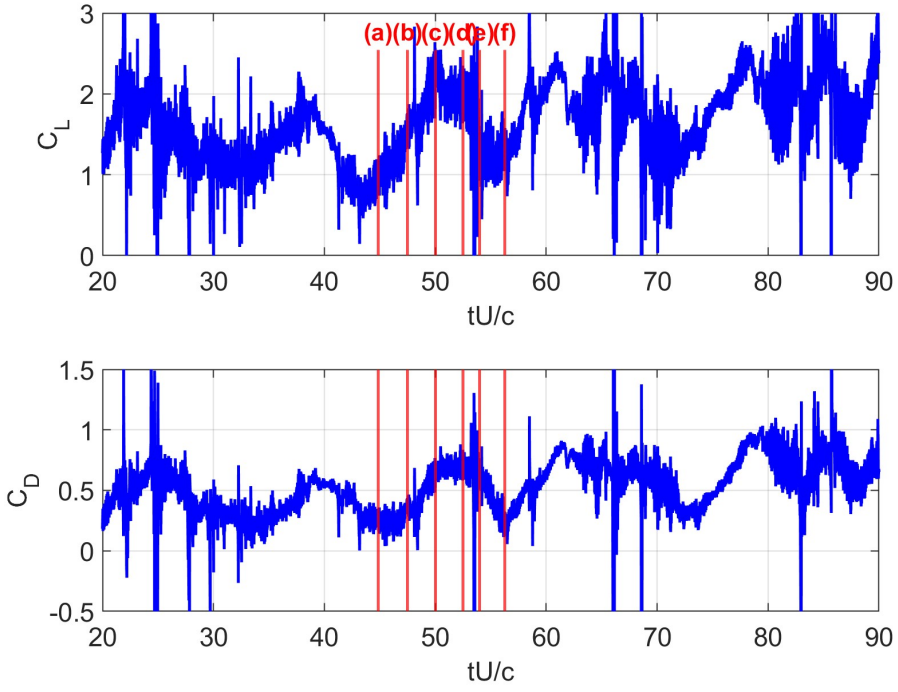

Figure 4.6: C_L and C_D values for the No PDF and $\Delta t = 2.5 \times 10^{-6}$ case

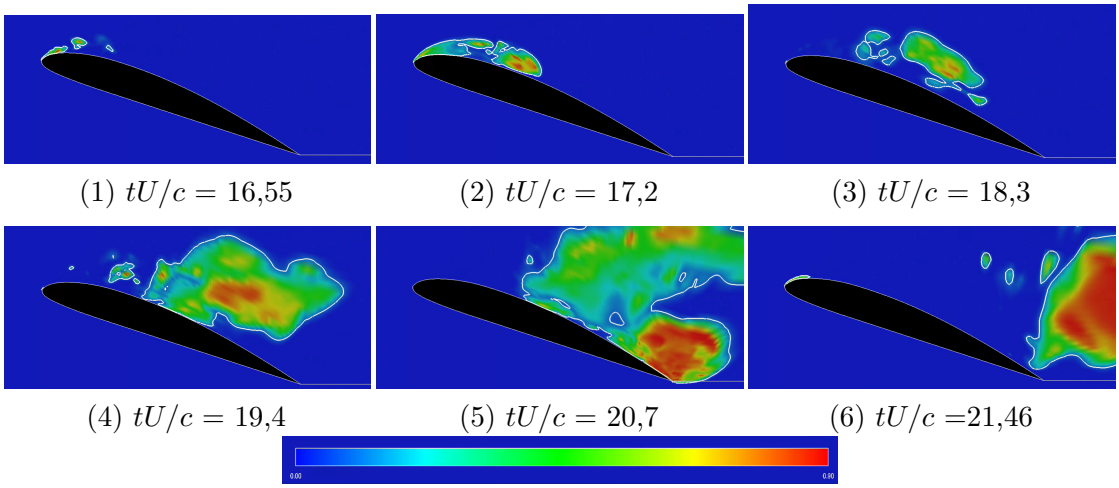

Figure 4.7: Cavitation cycle for C=5 case

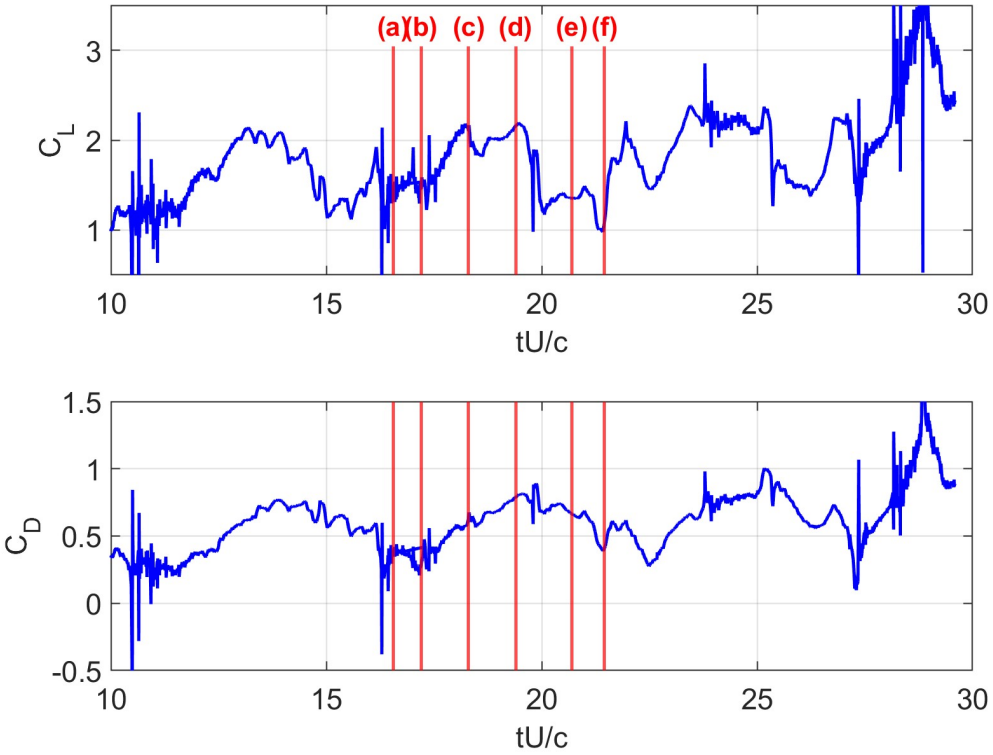

Figure 4.8: C_L and C_D values for C=5

In particular, here the comparison between a cycle corresponding to the No PDF $\Delta t = 2.5 \times 10^{-6}$ data (Fig. 4.5) and the PDF $C = 5$, $\Delta t = 5 \times 10^{-6}$ data (Fig. 4.7) can be seen.
In general, as expected, both cycles have a similar correspondence between the evolution of cavitation and the corresponding phase in the C_L graph. The peaks are linked to the moments when the cavity is reaching the maximum development in the leading edge area.
Conversely, the amount of cavitation and its temporal and spatial development are quite different. The No PDF case (Fig. 4.5) generates less cavity and is more confined in the trailing edge area compared to the PDF case (Fig. 4.7), especially in the moments when the cloud cavity generation should be at its maximum. Additionally, there are moments when cavitation disappears completely in the No PDF data. In contrast the PDF model is able to avoid the complete disappearence of the cavitating flow, making this simulation more similar to Kitamura's results [49]. However, though, also the PDF cases displays important differences compared to the experiment. The development of the cavitation is more unsteady and unpredictable in the PDF model.
As for the cases with $C = 10$, both for $\Delta t = 5 \times 10^{-6}$ and $\Delta t = 2.5 \times 10^{-6}$, it is very difficult to appreciate a real periodicity in the C_L and C_D graphs Figs. 4.9 and 4.10 thus it's also difficult to show a proper cavitation cycle.

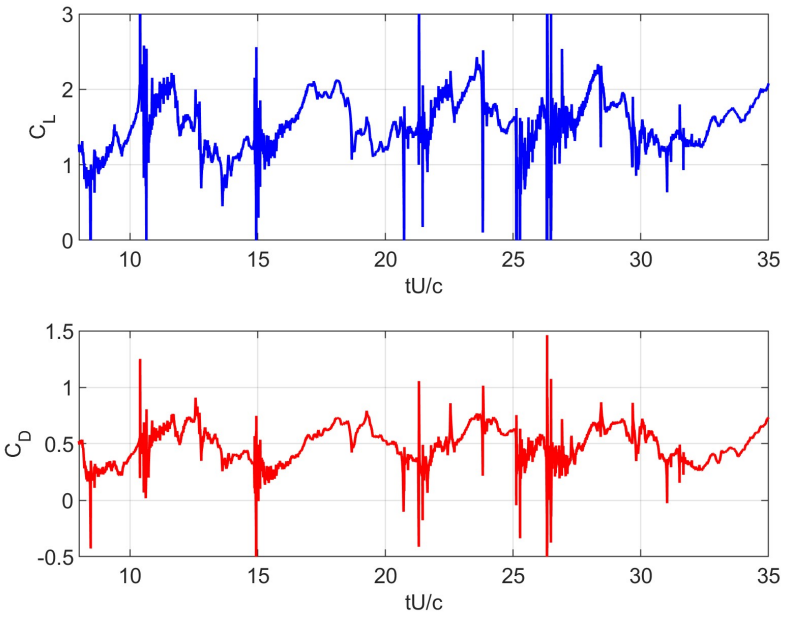

Figure 4.9: C_L and C_D values for the C=10 $\Delta t = 5 \times 10^{-6}$

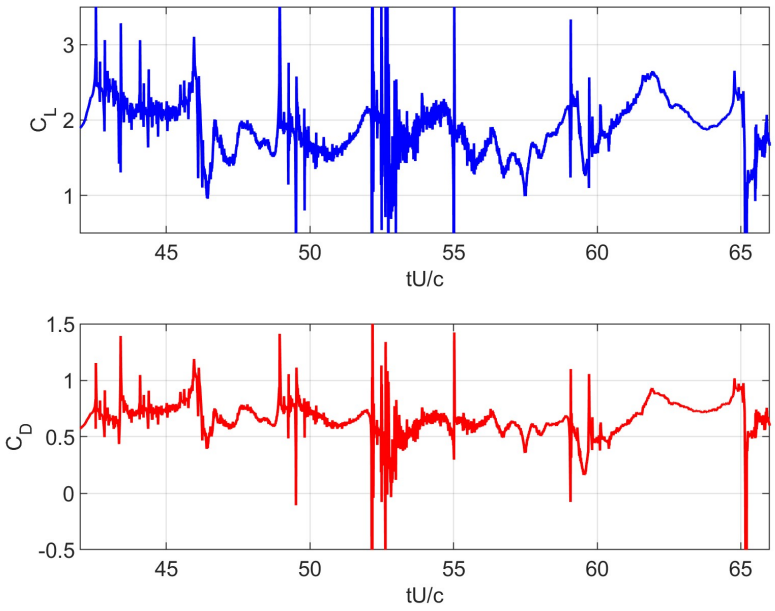

Figure 4.10: C_L and C_D values for the C=10 $\Delta t = 2.5 \times 10^{-6}$

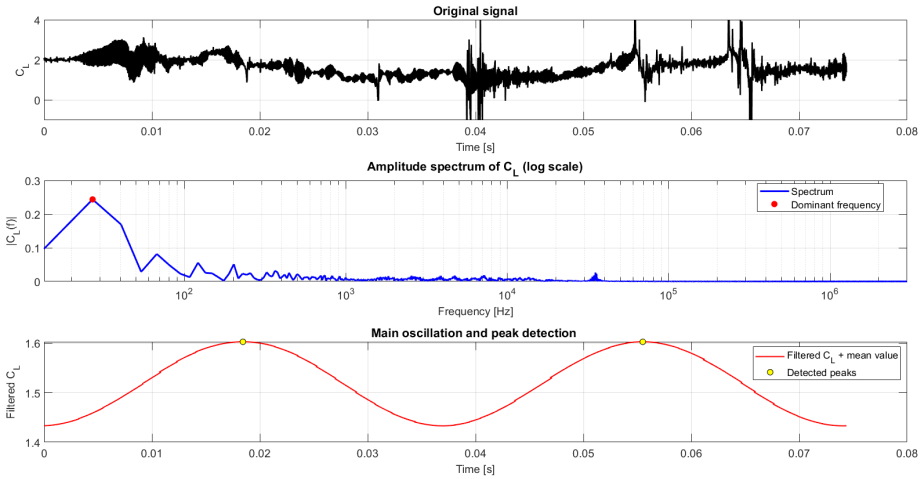

Figure 4.11: FFT No PDF $\Delta t = 2.5 \times 10^{-6}$

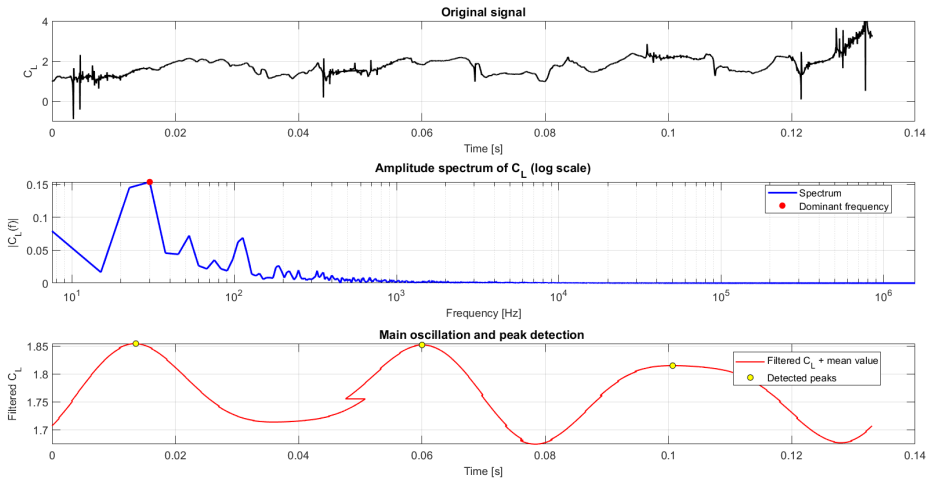

Figure 4.12: FFT C=5

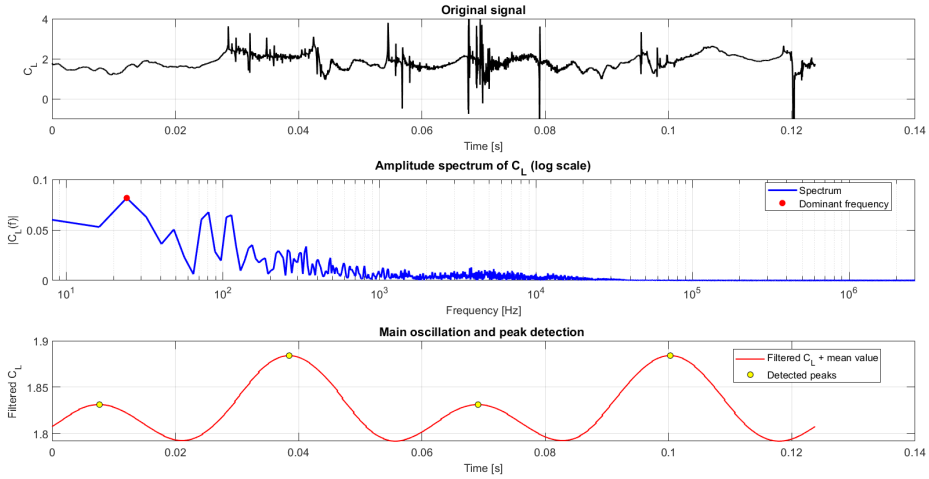

Figure 4.13: FFT C=10 $\Delta t = 2.5 \times 10^{-6}$

To gain a deeper understanding of the coefficient behavior, an FFT analysis was performed. Table 4.1 display the dominant frequency, theoretical periocity, adimensional periodicity and Strouhal number for each case and for Kitamura et al. experiment [49]. It is difficult to determine whether the PDF models lead to an improvement in the results. In particular, the experiments showed a Strouhal number of 0.17 for the $\sigma = 3.0$ case and 0.21 for the $\sigma = 2.0$ case. The PDF model with $C = 5$ and $\sigma = 2.7$, on the other hand, yielded a Strouhal number of 0.21,

whereas the No PDF case resulted in 0.19; this suggests that the No PDF case is likely more accurate than the former.

Table 4.1: Parameters of the FFT analysis

Case	f_{dom} [Hz]	**Theoretical Periodicity [s]**	**Adimensional Periodicity**	**Strouhal Number**
No PDF $dt = 2.5 \times 10^{-6}$	26.44538	0.037	5.31	0.1882
PDF C=5 $dt = 5 \times 10^{-6}$	30.07512	0.033	4.750	0.21053
PDF C=10 $dt = 2.5 \times 10^{-6}$	24.23987	0.041	5.090	0.19648
Kitamura's exp. ($\sigma = 3$)	-	-	-	0.17

4.3 Cell Volume at the trailing edge

While for $\alpha = 8$ ° the focus of attention was around the leading edge area, for the case $\alpha = 20°$ it develops more strongly around the trailing edge. Indeed cavitation does not develop as a long sheet cavity but consists of bubbles detaching from the second half of the wing profile in a more unstable and turbulent way.
The PDF model with $C = 5$ is able to slightly capture the link between the subgrid-scale cavity generation linked to Situation a) and the turbulent kinetic energy of SGS. This connection, however, is not captured in the PDF models with C=10, neither for $dt = 5 \times 10^{-6} s$ nor for $dt = 2.5 \times 10^{-6} s$.

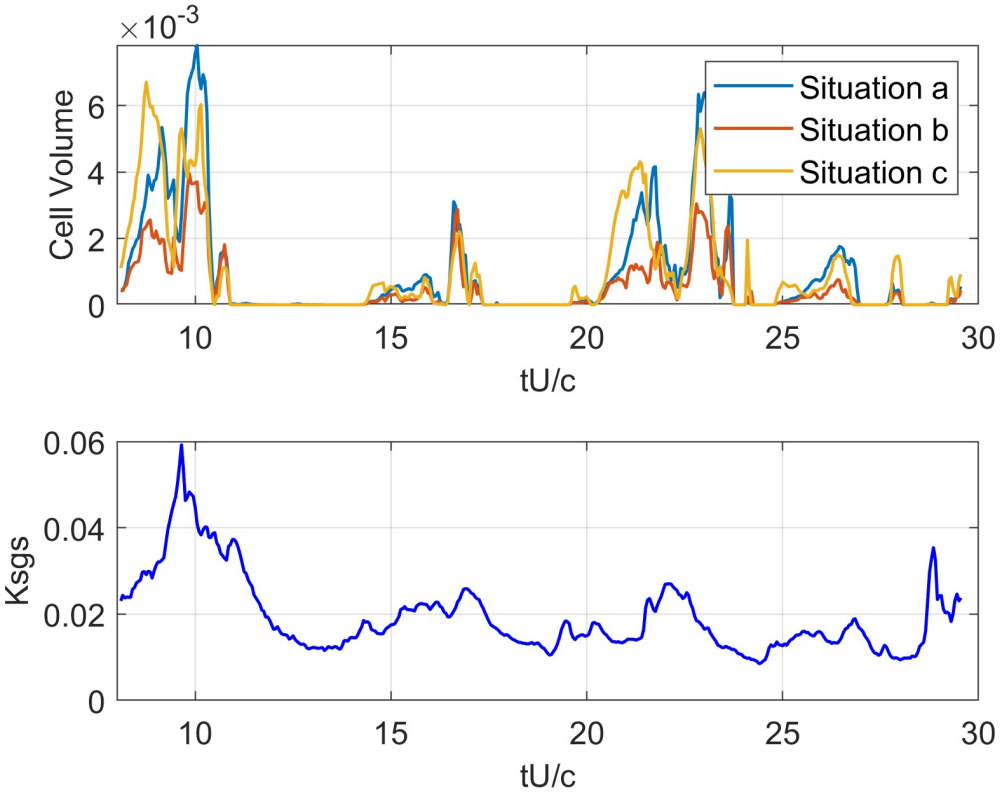

Figure 4.14: Cavity volume generation and K_{SGS} at the trailing edge for $C = 5$

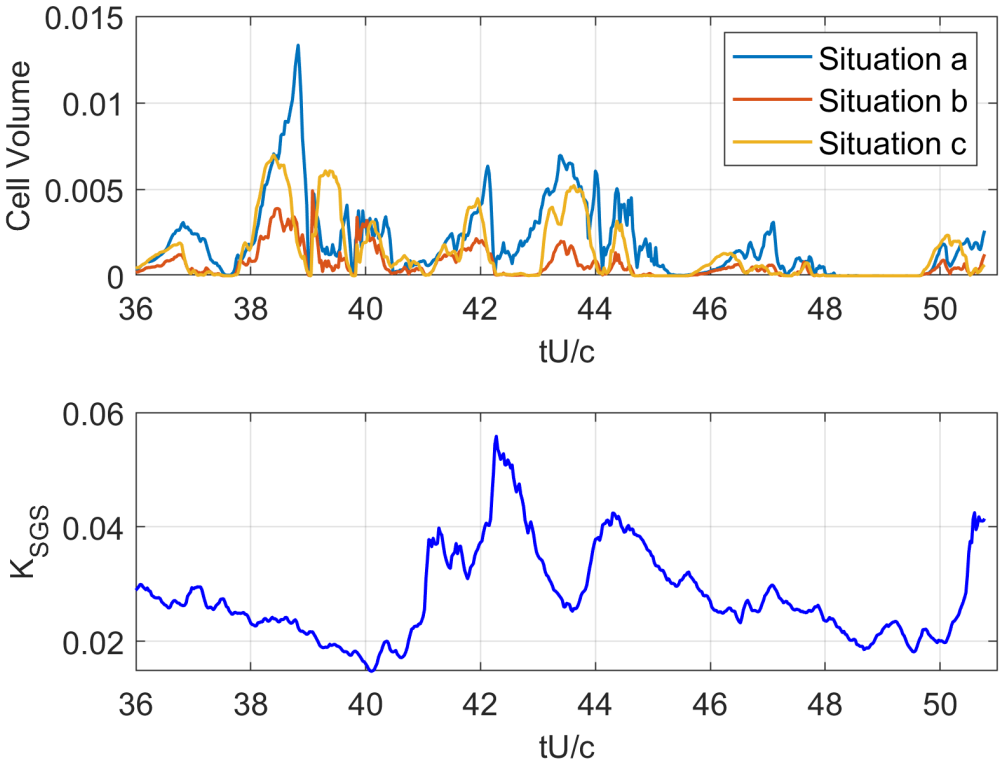

Figure 4.15: Cavity volume generation and K_{SGS} at the trailing edge for $C = 10$ $\Delta t = 2.5 \times 10^{-6}$

Chapter 5

Conclusions

The work presented in this thesis aimed at analysing the behavior of a cavitating flow around a Clark-Y11.7% hydrofoil through a LES approach modified by a PDF-based cavitation model. The introduction of this model was motivated by the idea that part of the vapor formation originates from the unresolved turbulent structures, which are normally treated in simplified ways through eddy viscosity. The possibility of representing the pressure fluctuations associated with the SGS vortices through a Gaussian distribution function offered a way to introduce additional cavity generation.

Two operating conditions were considered, corresponding to different flow regimes. The first one, where the profile presents a low angle of attack ($\alpha = 8°$, $\sigma = 1.2$) is closer to the classical sheet-to-cloud cavitation dynamics observed in many experimental studies. The second one, that present a higher angle of attack ($\alpha = 20°$, $\sigma = 2.7$) is instead characterized by a much stronger turbulent detachment and a cavitation that is mainly concentrated in the trailing edge area of the profile. The model was therefore tested under conditions that stress in different ways the interplay between turbulence and phase change.

5.1 Effectiveness of the PDF model

For the first configuration, the introduction of the PDF formulation clearly produced an improvement with respect to the standard LES cavitation model. The simulations showed a greater amount of cavity generation, especially the part associated with the probability of low-pressure excursions (Situation (a)), which does not appear at all in the classical homogeneous model. This resulted in a longer sheet cavity and in a behavior that is closer to the transitional oscillation observed in experiments [50].

The ability of the PDF model to prevent the complete disappearance of the

cavity, something that often occurs in traditional LES, represents an important improvement. The maximum sheet cavity length obtained with the PDF, particularly with the choice $C = 5$, matches reasonably well with the experimental references. Some small improvements were also observed in the pressure distribution, especially near the leading edge, where previous CFD approaches struggled to reproduce the initial flat region of the pressure coefficient.

From the point of view of the performance coefficients, the introduction of the PDF did not change the mean values of lift and drag, but it did influence the oscillatory behavior. The frequencies identified through FFT were closer to the experimental trends, and the flow field visualizations confirmed a more realistic succession of cavity growth, detachment and collapse.

Overall, for this flow regime the model appears to properly capture an important portion of the flow behavior that is missing in the classical LES cavitation approach.

5.2 Limitations

The second configuration led to considerably more complex dynamics. At $\alpha = 20°$, the flow separation is massive and the cavitation develops mainly as bubble-type or cloud-type structures around the trailing edge. For this reason, the improvements brought by the PDF model were less evident. Although the PDF still increased the total vapor content and avoided, in several instances, the full disappearance of cavitation, its correlation with the subgrid-scale kinetic energy was weaker, especially for the case $C = 10$. In fact, the use of a larger constant might amplify the unsteadiness in a non-physical way, and numerical stability issues required a reduction of the time step.

The analysis of lift and drag did not show a clear periodicity, especially for the $C = 10$ case, something that is instead seen in the experimental results. Unlike the first case, the PDF model did not provide an appreciable improvement in predicting the performance coefficients behavior.

This suggests that in highly separated flows the current formulation of the PDF model may not be sufficient to capture reliably the complex and large-scale turbulent structures that drive cavitation.

5.3 Considerations regarding C

An additional aspect that emerged from this study is the strong sensitivity of the results to the model constant C. While $C = 5$ provided a good balance between improved cavity generation and numerical robustness, the value $C = 10$ tended to exaggerate the standard deviation of the pressure PDF and, especially in the second case, compromised the correlation between SGS turbulence and vapor formation.

5.4 Possible future developments

The work carried out in this thesis naturally suggests several potential extensions. One direction could be the introduction of a variable or dynamically computed value of the constant C, possibly linked to local flow quantities. This might allow the model to automatically adapt to the characteristics of the resolved flow. Furthermore, a dedicated analysis of the instantaneous velocity field, especially aimed at identifying the re-entrant jet mechanism, could clarify several aspects of the cavity breakup mechanism and offer better validation for the model. Finally, applying the model to other cavitation regimes, such as vortex cavitation or tip vortices, could help determine whether the PDF approach is particularly suited for specific flow conditions and whether it can be integrated into more general cavitation modeling strategies.

5.5 Final remarks

In conclusion, the work confirmed that incorporating subgrid-scale fluctuations into a cavitation model can meaningfully improve the physical accuracy of LES simulations when the regime is between partial cavitation and transient cavitation. Although the model does not provide improvements under all conditions, its performance in the moderate-incidence case highlights the potential of this approach. The results obtained represent a promising step toward more comprehensive models capable of linking turbulence and cavitation at multiple scales.

Bibliography

[1] K. Okabayashi and T. Kajishima. «Large Eddy Simulation Study on the Relationship Between Large-scale Turbulence Vortices and Unsteady Cavitation Around a Hydrofoil». In: *Journal of Fluids Engineering* 145.4 (2023), pp. 041204–12. DOI: 10.1115/1.4056525 (cit. on pp. 1, 16, 18, 26, 42).

[2] Jean-Pierre Franc and Jean-Marc Michel. *Fundamentals of Cavitation*. Vol. 76. Fluid Mechanics and Its Applications. Dordrecht: Kluwer Academic Publishers, 2010. ISBN: 978-90-481-2982-2 (cit. on pp. 1, 2).

[3] T. S. Folden. «A classification and review of cavitation models with an emphasis on physical aspects of cavitation». In: *arXiv preprint* (2022). arXiv:2211.16323 [physics.flu-dyn]. DOI: 10.48550/arXiv.2211.16323. eprint: 2211.16323 (cit. on p. 1).

[4] Kie Okabayashi. « LES». , PhD thesis. Osaka University, Mar. 2011. URL: https://hdl.handle.net/11094/2307 (cit. on pp. 1, 3, 7, 12, 13, 16, 42).

[5] K. Yasuda. «Decomposition of Chemical Substances by Ultrasound and Development of Ultrasonic Reactors». Japanese. In: *The Chemical Times* 2 (2009). No. 212 (total issue), pp. 2–7 (cit. on p. 1).

[6] H. Hashiba, T. Kawabata, K. Masuzawa, K. Umemura, M. Kimata, and S. Maeda. «Inactivation of Cryptosporidium by Ultrasonic Cavitation Using the Squeeze Film Effect». Japanese. In: *Proceedings of the 11th Symposium on Cavitation*. Japan, 2001, pp. 171–174 (cit. on p. 1).

[7] F. Moriyasu. «Ultrasound Imaging Using Microbubbles as Contrast Agents». Japanese. In: *Proceedings of the 11th Symposium on Cavitation*. Japan, 2001, pp. 17–18 (cit. on p. 1).

[8] T. Kawabata, R. Asami, H. Azuma, K. Sasaki, and K. Umemura. «Ultrasound Diagnosis and Therapy Using Microbubble Generation from Nanodroplets». Japanese. In: *Proceedings of the 14th Symposium on Cavitation*. Paper No. 44. Japan, 2009 (cit. on p. 1).

[9] Ebrahim Ghahramani, Henrik Ström, and Rickard E. Bensow. «Numerical simulation and analysis of multi-scale cavitating flows». In: *Journal of Fluid Mechanics* 922 (2021), A22. DOI: 10.1017/jfm.2021.424. URL: https://doi.org/10.1017/jfm.2021.424 (cit. on p. 2).

[10] J. P. Franc and J. M. Michel. «Attached cavitation and the boundary layer: experimental investigation and numerical treatment». In: *Journal of Fluid Mechanics* 193 (1988), pp. 63–84. DOI: 10.1017/S0022112088002107. URL: https://doi.org/10.1017/S0022112088002107 (cit. on p. 3).

[11] American Society of Mechanical Engineers. «Two Phase Flow Approach in Unsteady Cavitation Modelling». In: *ASME Fluids Engineering Division, FED*. Vol. 98. Conference Paper, EID: 2-s2.0-0025568267. 1990, pp. 153–158 (cit. on p. 3).

[12] Charles L. Merkle, Jie Feng, and Paul E. O. Buelow. «Computational Modeling of Dynamics of Sheet Cavitation». In: *Proceedings of the 3rd International Symposium on Cavitation (CAV1998)*. 1998, pp. 307–311 (cit. on p. 3).

[13] R. F. Kunz, D. A. Boger, D. R. Stinebring, T. S. Chyczewski, J. W. Lindau, H. J. Gibeling, S. Venkateswaran, and T. R. Govindan. «A Preconditioned Navier–Stokes Method for Two-Phase Flows with Application to Cavitation Prediction». In: *Computers & Fluids* 29.8 (2000), pp. 849–875. DOI: 10.1016/S0045-7930(99)00039-0. URL: https://doi.org/10.1016/S0045-7930(99)00039-0 (cit. on p. 3).

[14] Ashok K. Singhal, Mahesh M. Athavale, Huiying Li, and Yu Jiang. «Mathematical Basis and Validation of the Full Cavitation Model». In: *Journal of Fluids Engineering* 124.3 (2002), pp. 617–624. DOI: 10.1115/1.1486223. URL: https://doi.org/10.1115/1.1486223 (cit. on p. 3).

[15] G. H. Schnerr and Jürgen Sauer. «Physical and Numerical Modeling of Unsteady Cavitation Dynamics». In: *Proceedings of the 4th International Conference on Multiphase Flow (ICMF 2001)*. New Orleans, USA, 2001 (cit. on p. 3).

[16] P. J. Zwart, A. G. Gerber, and T. Belamri. «A Two-Phase Flow Model for Predicting Cavitation Dynamics». In: *Proceedings of the 5th International Conference on Multiphase Flow (ICMF 2004)*. Vol. 152. 2004, pp. 1–11 (cit. on p. 3).

[17] Y. Ito, K. Sawasaki, N. Tani, T. Nagasaki, and T. Nagashima. «A Blowdown Cryogenic Cavitation Tunnel and CFD Treatment for Flow Visualization Around a Foil». In: *Journal of Thermal Science* 14 (2005), pp. 346–351. DOI: 10.1007/s11630-005-0056-5. URL: https://doi.org/10.1007/s11630-005-0056-5 (cit. on p. 3).

[18] Y. Tamura and Y. Matsumoto. «Improvement of Bubble Model for Cavitating Flow Simulations». In: *Journal of Hydrodynamics* 21.1 (2009), pp. 41–46. DOI: 10.1016/S1001-6058(08)60117-1. URL: https://doi.org/10.1016/S1001-6058(08)60117-1 (cit. on p. 3).

[19] C. T. Hsiao, G. L. Chahine, and H. L. Liu. «Scaling effect on prediction of cavitation inception in a line vortex flow». In: *Journal of Fluids Engineering* 125.1 (2003), pp. 53–60. DOI: 10.1115/1.1521956 (cit. on p. 4).

[20] Shungo Okamura and Kie Okabayashi. «Twin experiments for data assimilation of cavitating flow around a hydrofoil». In: *International Journal of Multiphase Flow* 188 (2025), p. 105201. DOI: 10.1016/j.ijmultiphaseflow.2025.105201. URL: https://doi.org/10.1016/j.ijmultiphaseflow.2025.105201 (cit. on p. 4).

[21] Robert F. Kunz, Jules Washington Lindau, Todd A. Kaday, and Leonard Joel Peltier. «Unsteady RANS and Detached Eddy Simulations of cavitating flow over a hydrofoil». In: *Proceeding of the 5th International Symposium on Cavitation (CAV2003)*. 2003. URL: https://api.semanticscholar.org/CorpusID:54587879 (cit. on pp. 4, 18).

[22] A. K. Singhal, N. Vaidya, and A. D. Leonard. «Multi-dimensional simulation of cavitating flows using a PDF model for phase change». In: *Proceedings of the ASME FEDSM97, Forum on Cavitation and Multiphase Flow*. FEDSM'97. CFD Research Corporation. Vancouver, Canada, 1997, p. 3272 (cit. on pp. 4, 11, 18).

[23] Olivier Coutier-Delgosha, Regiane Fortes-Patella, and Jean-Luc Reboud. «Evaluation of the Turbulence Model Influence on the Numerical Simulations of Unsteady Cavitation». In: *Journal of Fluids Engineering* 125.1 (2003), pp. 38–45. DOI: 10.1115/1.1524584. URL: https://doi.org/10.1115/1.1524584 (cit. on p. 4).

[24] Olivier Coutier-Delgosha, Jean-Louis Reboud, and Yves Delannoy. «Numerical Simulation of the Unsteady Behaviour of Cavitating Flows». In: *International Journal for Numerical Methods in Fluids* 42.5 (2003), pp. 527–548 (cit. on p. 4).

[25] Jianjun Wu, Guoping Wang, and Wei Shyy. «Time-Dependent Turbulent Cavitating Flow Computations With Interfacial Transport and Filter-Based Models». In: *International Journal for Numerical Methods in Fluids* 49.7 (2005), pp. 739–761 (cit. on p. 4).

[26] Massimo Germano, Ugo Piomelli, Parviz Moin, and William H. Cabot. «A Dynamic Subgrid-Scale Eddy Viscosity Model». In: *Physics of Fluids A* 3.7 (1991), pp. 1760–1765 (cit. on pp. 4, 5, 10).

[27] Q. Qin. «Numerical Modeling of Natural and Ventilated Cavitating Flows». Doctoral Thesis. Minneapolis, MN, USA: University of Minnesota, 2004 (cit. on p. 5).

[28] M. Wosnik, Q. Qin, and R. E. A. Arndt. «Identification of Large-Scale Structures in the Wake of Cavitating Hydrofoils Using LES and Time-Resolved PIV». In: *Proceedings of the 6th International Symposium on Cavitation (CAV2006)*. Wageningen, The Netherlands, 2006 (cit. on p. 5).

[29] F. Nicoud and F. Ducros. «Subgrid-Scale Stress Modeling Based on the Square of the Velocity Gradient Tensor». In: *Flow, Turbulence and Combustion* 62.3 (1999), pp. 183–200 (cit. on p. 5).

[30] G. Wang and M. Ostoja-Starzewski. «Large-Eddy Simulation of a Sheet/Cloud Cavitation on a NACA0015 Hydrofoil». In: *Applied Mathematical Modelling* 31.3 (2007), pp. 417–447 (cit. on p. 5).

[31] K. Yamade, H. Kato, K. Tani, and T. Yamanishi. «LES Analysis of Cavitation Flow Around Two-Dimensional Objects». In: *Proceedings of the 18th Symposium on Computational Fluid Dynamics*. Japan, 2004 (cit. on p. 5).

[32] Kohei Okita and Takeo Kajishima. «Three-Dimensional Computation of Unsteady Cavitating Flow in a Cascade». In: *Proceedings of the 9th International Symposium on Transport Phenomena and Dynamics of Rotating Machinery (ISROMAC-9)*. (CD-ROM), Paper No. FD-ABS-076. Honolulu, Hawaii, USA, 2002 (cit. on p. 5).

[33] E. Shams and S. Apte. «Large Eddy Simulation of Cavitation Inception in a High Speed Flow Over an Open Cavity». In: *Proceedings of the 7th International Symposium on Cavitation (CAV2009)*. Ann Arbor, MI, USA, Aug. 2009, pp. 1–16 (cit. on p. 5).

[34] X. Liu and J. Katz. «Cavitation Phenomenon Occurring due to Interaction of Shear Layer Vortices with the Trailing Corner of a Two-Dimensional Open Cavity». In: *Physics of Fluids* 20.4 (2008) (cit. on p. 5).

[35] N. Dittakavi, A. Chunekar, and S. Frankel. «Large Eddy Simulation of Turbulent-Cavitation Interactions in a Venturi Nozzle». In: *ASME Journal of Fluids Engineering* 132.12 (2010), pp. 1–11 (cit. on p. 5).

[36] B. Ji, X. W. Luo, R. E. A. Arndt, X. Peng, and Y. Wu. «Large Eddy Simulation and Theoretical Investigations of the Transient Cavitating Vortical Flow Structure Around a NACA66 Hydrofoil». In: *International Journal of Multiphase Flow* 68 (2015), pp. 121–134 (cit. on p. 5).

[37] A. Gnanaskandan and K. Mahesh. «A Numerical Method to Simulate Turbulent Cavitating Flows». In: *International Journal of Multiphase Flow* 70 (2015), pp. 22–34 (cit. on p. 5).

[38] T. Suzuki, Y. Yamade, and C. Kato. «Accuracy Validation of Cavitation Performance Prediction for Single Hydrofoil by LES». In: *Seisan Kenkyu* 63.1 (2011), pp. 55–60 (cit. on p. 5).

[39] M.-R. Pendar and E. Roohi. «Cavitation Characteristics Around a Sphere: An LES Investigation». In: *International Journal of Multiphase Flow* 98 (2018), pp. 1–23 (cit. on p. 5).

[40] H. Ugajin, M. Kawai, K. Okita, T. Ohta, T. Kajishima, M. Nakano, and H. Tomaru. «Unsteady RANS and Detached Eddy Simulations of Cavitating Flow Over a Hydrofoil». In: *AIAA Paper*. AIAA Paper No. 2007-5535. 2007 (cit. on pp. 5, 18).

[41] P. R. Spalart, W. H. Jou, M. Strelets, and S. R. Allmaras. «Comments on the feasibility of LES for Wings, and on a Hybrid RANS/LES Approach». In: *Proc. 1st AFOSR International Conference on DNS/LES*. 1997, pp. 137–147 (cit. on p. 5).

[42] Masayoshi Okamoto and Nobuyuki Shima. «Investigation for the One-Equation-Type Subgrid Model with Eddy-Viscosity Expression Including the Shear-Damping Effect». In: *JSME International Journal Series B : Fluids and Thermal Engineering* 42.2 (1999), pp. 154–161. DOI: 10.1299/jsmeb.42.154. URL: https://doi.org/10.1299/jsmeb.42.154 (cit. on p. 10).

[43] Douglas K. Lilly. «A Proposed Modification of the Germano Subgrid-Scale Closure Method». In: *Physics of Fluids A* 4.3 (1992), pp. 633–635 (cit. on p. 10).

[44] Nobuyuki Kajishima. «One-Equation Subgrid Scale Model Using Dynamic Procedure for the Energy Production». In: *Journal of Applied Mechanics* 73.3 (2006), pp. 368–374. DOI: 10.1115/1.2164509. URL: https://doi.org/10.1115/1.2164509 (cit. on p. 10).

[45] Kohei Okita and Takeo Kajishima. «Numerical Simulation of Unsteady Cavitating Flow around a Hydrofoil». In: *Transactions of the Japan Society of Mechanical Engineers, Series B* 68.667 (2002), pp. 637–644. DOI: 10.1299/kikaib.68.637. URL: https://doi.org/10.1299/kikaib.68.637 (cit. on p. 10).

[46] J. O. Hinze. *Turbulence*. 2nd. McGraw-Hill, 1975, p. 309 (cit. on p. 13).

[47] Kie Okabayashi and Takeo Kajishima. «Modeling of the Subgrid-Scale Pressure Distribution in Turbulent Mixing Layer». In: *Journal of Fluid Science and Technology* 6.1 (2011), pp. 73–84. DOI: 10.1299/jfst.6.73 (cit. on p. 13).

[48] J. P. Franc and J. M. Michel. «Attached cavitation and the boundary layer: experimental investigation and numerical treatment». In: *Journal of Fluid Mechanics* 154 (1985), pp. 63–90. DOI: 10.1017/S0022112085001458. URL: https://doi.org/10.1017/S0022112085001458 (cit. on p. 17).

[49] Soichiro Kitamura, Wakana Tsuru, and Hiroshi Watanabe. «Lift and Drag Forces around Clark Y Hydrofoil under Cavitating Flow at Multiple Angles of Attack with Different Boundary Layer Characteristics». In: *Physics of Fluids* 35.12 (2023), p. 127107. DOI: 10.1063/5.0146697. URL: https://doi.org/10.1063/5.0146697 (cit. on pp. 18, 49, 52, 54).

[50] Satoshi Watanabe, Naoto Suefuji, Wataru Yamaoka, and Akinori Furukawa. «Lift and Drag Characteristics of a Cavitating Clark-Y 11.7% Hydrofoil». In: *Turbomachinery* 41.7 (2013), pp. 440–446. DOI: 10.1299/jts.41.440. URL: https://www.jstage.jst.go.jp/article/tsj/41/7/41_440/_article/-char/en (cit. on pp. 18, 31, 33, 58).

[51] F. Numachi, K. Tsunoda, and I. Senda. «Cavitation Tests on Six Profiles for Blade Elements». In: *Report of the Institute of High Speed Mechanics* 1.1 (1949). In Japanese, pp. 1–16 (cit. on p. 18).

[52] H. Murai, Y. Hirata, and Y. Mikajima. «Research on Swept-Back Blades Laid Between Parallel Walls (Report 1)—Experimental Research on Clark-y11.7% Blade with Aspect Ratio of 2.0». In: *Report of the Institute of High Speed Mechanics* 21.210 (1965). In Japanese, pp. 183–200 (cit. on p. 18).

[53] Chisachi Kato. *Final Report of Turbomachinery Society of Japan Consortium Project—Advancement of CFD Prediction of Cavitation in Turbomachinery*. Technical Report. Tokyo, Japan: Turbomachinery Society of Japan, 2011, pp. 1–9 (cit. on pp. 26, 41).

[54] Chisachi Kato. *Final Report of Turbomachinery Society of Japan Consortium Project—Advancement of CFD Prediction of Cavitation in Turbomachinery*. Technical Report. In Japanese. Tokyo, Japan: Turbomachinery Society of Japan, 2011, pp. 1–9 (cit. on p. 26).

[55] Chisachi Kato. «Industry–University Collaborative Project on Numerical Predictions of Cavitating Flows in Hydraulic Machinery: Part 1—Benchmark Test on Cavitating Hydrofoils». In: *Proceedings of the ASME/JSME 2011 Joint Fluids Engineering Conference (AJK2011-FED)*. ASME Paper No. AJK2011-06084. 2011 (cit. on p. 26).

[56] Alan V. Oppenheim and Ronald W. Schafer. *Discrete-Time Signal Processing*. 2nd. Prentice Hall, 1999. ISBN: 978-0137549207 (cit. on p. 30).

[57] Peter D. Welch. «The use of Fast Fourier Transform for the estimation of power spectra: a method based on time averaging over short, modified periodograms». In: *IEEE Transactions on Audio and Electroacoustics* 15.2 (1967), pp. 70–73. DOI: 10.1109/TAU.1967.1161901 (cit. on p. 30).

[58] Anatol Roshko. «On the Development of Turbulent Wakes from Vortex Streets». In: *NACA Report* 1191 (1954) (cit. on p. 30).

[59] C. H. K. Williamson. «Vortex dynamics in the cylinder wake». In: *Annual Review of Fluid Mechanics* 28.1 (1996), pp. 477–539 (cit. on p. 30).

[60] T. M. Currier, A. J. Smits, and H. Dong. «Dynamics of a hydrofoil free to oscillate in the wake of a fixed, constantly rotating or periodically rotating cylinder». In: *Journal of Fluid Mechanics* 916 (2021), A25 (cit. on p. 31).

[61] C. Cai. «Numerical investigations of hydrodynamic performance of hydrofoil». In: *Advances in Mechanical Engineering* 7.8 (2015), pp. 1–11. DOI: 10.1177/1687814015592088 (cit. on p. 31).

[62] E. Hua, L. Zhang, and D. Wu. «Comparative Analysis of Hydrodynamic Performance for Hydrofoil Motion». In: *Micromachines* 10.8 (2025), p. 549. DOI: 10.3390/mi10080549 (cit. on p. 31).